OLED devices optimization for lighting application

Salvatore Aprano

Unione Europea

Ministero dell'Istruzione, dell'Università e della Ricerca

UNIVERSITÀ DEGLI
STUDI DI SALERNO

FONDO SOCIALE EUROPEO
Programma Operativo Nazionale 2000/2006
"Ricerca Scientifica, Sviluppo Tecnologico, Alta Formazione"
Regioni dell'Obiettivo 1 – Misura III.4
"Formazione superiore ed universitaria"

Department of Industrial Engineering

Ph.D. Course in Electronic Engineering
(XV Cycle-New Series, XXIX Cycle)

OLED devices optimization for lighting
application

Supervisor	**Ph.D. student**
Prof. Alfredo Rubino	*Salvatore Aprano*
Dott.sa Maria Grazia Maglione	

Scientific Referees
Prof. Alessandro Pezzella
Dott. Mario Barra

Ph.D. Course Coordinator
Prof. Ernesto Reverchon

*"It is during our darkest moments
that we must focus to see
the light."*

-Alexander Onassis-

Scientific Works

- "Eumelanin-PEDOT:PSS complementing en route to mammalian pigment based-electrodes: design and fabrication of ITO-free organic light emitting device", L. Migliaccio, S. Aprano, L. Iannuzzi, M. G. Maglione, P. Tassini, C. Minarini, P. Manini and A. Pezzella, *Advanced Electronic Materials*, accepted

- "Gravure printed PEDOT:PSS as anode for flexible ITO-free organic light emitting diodes", M. Montanino, G. Sico, T. Prontera, A. De Girolamo Del Mauro, S. Aprano, M. G. Maglione, C. Minarini, *eXPRESS Polymer Letters*, accepted.

- "Electron Beam Curing Technology for Very High Throughput Manufacturing of Flexible Alternating Current Powder Electroluminescent Devices", G. Sico, S. Aprano, P. Tassini, M. G. Maglione, E. Santoro, A. Rubino, C. Minarini, Electron Devices, *IEEE Trans. Electron Dev.* 63 (2), 710-716 (2016), ISNN: 0018-9383.

- Fotonica AEIT Italian Conference on Photonics Technologies, 2015, "Evaluation of the stability of different encapsulated blue OLEDs", E. Santoro, S. Aprano, G. Sico, M.R. Fiorillo, M. G. Maglione, P. Tassini, A. Rubino, C. Minarini, ISBN: 978-1-78561-068-4.

- "Eumelanin-PEDOT:PSS complementing en route to mammalian pigment based-electrodes: design and fabrication of ITO-free organic light emitting device", L. Migliaccio, S. Aprano, L. Iannuzzi, M. G. Maglione, P. Tassini, C. Minarini, P. Manini and A. Pezzella, *Advanced Electronic Materials*, accepted.

- "Gravure printed PEDOT:PSS as anode for flexible ITO-free organic light emitting diodes", M. Montanino, G. Sico, T. Prontera, A. De Girolamo Del Mauro, S. Aprano, M. G. Maglione, C. Minarini, *eXPRESS Polymer Letters*, accepted.

- "Electron Beam Curing Technology for Very High Throughput Manufacturing of Flexible Alternating Current Powder

Electroluminescent Devices", G. Sico, S. Aprano, P. Tassini, M. G. Maglione, E. Santoro,A. Rubino, C. Minarini, Electron Devices, *IEEE Trans. Electron Dev.* 63 (2), 710-716 (2016), ISNN: 0018-9383.

- Fotonica AEIT Italian Conference on Photonics Technologies, 2015, "Evaluation of the stability of different encapsulated blue OLEDs", E. Santoro, S. Aprano, G. Sico, M.R. Fiorillo, M. G. Maglione, P. Tassini, A. Rubino, C. Minarini, ISBN: 978-1-78561-068-4.

- "Synthesis, characterization, and use as emissive layer of white organic light emitting diodes of the highly isotactic poly(N-pentenyl-carbazole)", Botta, A., Pragliola, S., Venditto, V., A. Rubino,S. Aprano, A. De Girolamo Del Mauro, M. G. Maglione, C. Minarini, *Polymer Composites*, Vol. 36, Issue 6, 1110-1117 (2015), ISSN: 02728397

- "Dispositivi luminescenti OLED per applicazioni di illuminazione", M. G. Maglione, S. Aprano, P. Tassini, V. Criscuolo, T. Prontera, A. Rubino, P. Manini, C. Minarini (2015), *Energia Ambiente Innovazione – Speciale EAI*-ENEA - DOI 10.12910/EAI2015-094.

- "Un microcosmo per l'allevamento di piante in condizioni controllate", d'Aquino L., Maglione M. G., Lanza B., Atrigna M., De Filippo G., Pandolfi G., Giannotta G., Pedicini A., Aprano S., Minarini C., 2015. *Energia Ambiente Innovazione - Speciale III -* 2015 ENEA per EXPO 2015, 98-99.

- LOPE-C 2015, marzo 2015, München, Germany ,
  Poster: Aprano S., Maglione M. G., Cotella G. F., Bezzeccheri E., Prontera C. T., Criscuolo V., Pandolfi G., Tassini P., Rubino A. and Minarini C., "Blue fluorescence from α-NPD for a deeper blue spectral content in simplified hybrid fluorescent-phosphorescent OLEDs".

- GE 2015, 22- 24 June, Siena (ITALY),
  Poster:"Study and fabrication of selected organic electronic devices to improve performance and stability", S. Aprano, E. Bezzeccheri, M. R. Fiorillo, R. Liguori, E. Santoro, A. Rubino, C. Diletto , M. G. Maglione , G. Sico , P. Tassini , C. Minarini.

- TOP Conference Ischia, Italy, 22–26 June 2014, "Highly isotactic poly(N-pentenyl-carbazole): A challenging polymer for optoelectronic applications", *AIP Conf. Proc.* 1599, 493 (2014). Antonio Botta, Stefania Pragliola, Vincenzo Venditto, Alfredo Rubino, Salvatore Aprano, Anna De Girolamo Del Mauro, Maria Grazia Maglione, and Carla Minarini.

- E-MRS 2014 Spring Meeting Lille, France – 26- 30 May 2014, "Hybrid OLEDs based on quantum dots and polyfluorene", T. Di Luccio, S. Aprano, C. Borriello, A. Bruno, M. G. Maglione, C. Minarini,

- "Photo- and electroluminescent properties of bithiophene disubstituted 1,3,4-thiadiazoles and their application as active components in organic light emitting diodes", *Optical Materials*, vol.37, Pages 193–199, November 2014. Remigiusz Grykien, Beata Luszczynska, Ireneusz Glowacki, Ewa Kurach, Renata Rybakiewicz, Kamil Kotwica, Malgorzata Zagorska, Adam Pron, Paolo Tassini, Maria Grazia Maglione, Anna De Girolamo Del Mauro, Tommaso Fasolino, Romina Rega, Giuseppe Pandolfi, Carla Minarini, Salvatore Aprano.

List of contents

List of Figures

III

List of Tables

x

Abstract

In this work a potential new OLED application is presented: a large-area purple OLED for horticultural application, which combines red and blue light emissions in a unique device.

The main issue of this thesis is to demonstrate the effectiveness of the proposed OLED structure by using theoretical models created during the three years of the Ph.D. studies and applied to commercial materials.

The core of this dissertation is the third chapter, where the reader is brought to the optimization of the final purple OLED structure after several experiments, which confirm either the basic concepts explained in the two previous chapters, either a mathematical model for a fine-tuning of the blue emission layer.

Behind the proposed device architecture and material employed, there is the concept of "hybrid OLEDs with triplet harvesting", where a proper combined use of fluorescent and phosphorescent emitting materials allows a theoretical internal quantum efficiency of 100%.

The last chapter is focused on the study and the realization of metal grids on the indium-tin-oxide (ITO), which is the most used material as transparent and conductive anode for the OLED devices.

Despite ITO owns good property of transmittance (transparency), because of its limited conductivity, a lateral voltage drop occurs, preventing a homogeneous emission when the dimensions of the devices exceeds few square centimetres.

To overcome this problem, it is presented a new mathematical model which, unlike the most established literature models do, takes into account both the electrical influence of the metal grid and that one of the ITO.

Finally, with a good agreement with the experimental data, the theoretical model is used to predict optical and electrical behaviour of different hexagonal metal grid on ITO.

It worth to underline that all the approaches implemented in this work to achieve a large-area purple OLED, have a general validity. Indeed, the entire know-how in this thesis it has been successfully used, in the last three years,

to make several different OLED devices, different for colour emission, size and performances.

XII

Introduction

Organic light emitting diodes (OLEDs) have attracted, in the last thirty years, considerable research interest due to their potential to be used in next generation flat panel displays and low-cost solid state lighting.

The first electroluminescence (EL) in organic materials was observed by Helfrich and Schneider from anthracene in National Research Council, Canada in 1965 (W. Helfrich, 1965)., However no practical application of this technology was seen to be possible due to its extremely high operation voltage (~ 100 V).

The first work that combined modern thin film deposition techniques with suitable materials and structure, to give a moderately low bias voltage, was made by C.W. Tang and S. VanSlyke at Kodak, who introduced the double layer concept in 1987 (C. W. Tang, 1987). Their devices were made by subliming molecules of a triarylamine as hole transporter, followed by aluminato-tris-8-hydroxyquinolate (Alq3) for electron injection and light generation, and a magnesium-silver alloy cathode (Figure 1).
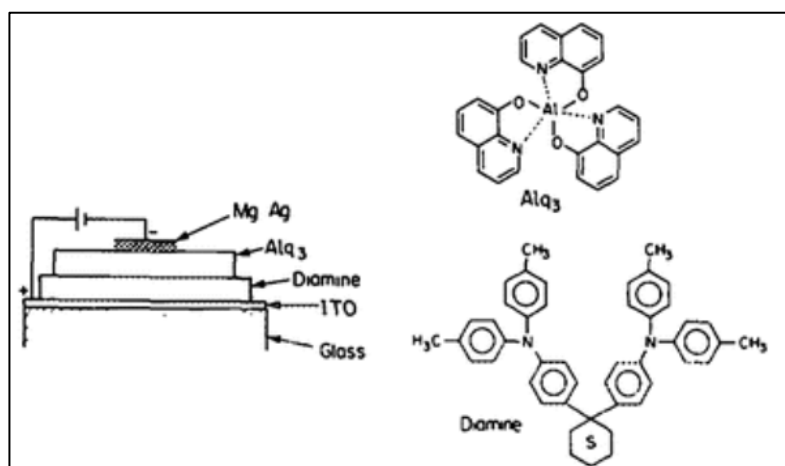
Figure 1 *Configuration of EL cell and molecular structure*

The Tang and VanSlyke's work is a milestone in the organic electronics. The concept of heterostructure has become a standard practice in OLEDs design, and is still adopted nowadays, thirty years later.

Single-layer devices tend to produce unbalanced charge injection and consequently low efficiency of light generation. Instead, using a charge transport or injection layer for holes and one for the electrons, the injected charges from the cathode and the anode are accumulated at the heterojunction, considerably increasing the probability of the electron-hole recombination at this organic/organic interface , which results in the reasonably high efficiency of radiative recombination of this type of devices.

Another major breakthrough in OLEDs technology was the fabrication of electrophosphorescent devices, accomplished by Baldo et al. (M. A. Baldo, D. F. O'Brien, Y. You, A. Shoustikov, S. Sibley, M. E. Thompson, and S. R. Forrest, Nature 395, 151 (1998).): these devices significantly increased the internal quantum efficiency as compared to the previous fluorescent devices. Using a phosphorescent dopant in a guest-host system, a nearly 100% internal quantum efficiency can be achieved (see chapter 1).

In terms of applications, the first commercialization of a product based upon the OLEDs was realized by Pioneer® in 1997 - producing the first generation of OLED display. About 10 years later, in 2008, SONY® launched the first commercial OLED TV (11 inches). LG launched the word's first 55 inches OLED TV at Consumer Electronics Show 2012, setting the future direction of the OLED display market.

Nowadays, the OLED display market is dominated by Samsung and LG. Indeed, OLED technology has recently gained significant market share in the display market. OLED displays are now mass produced for mobile phones, tablets, TVs, and wearables. IDTechEx (www.idtechex.com/) forecasts that market for all types of OLED displays will grow to $57bn in 2026.

The latest evolution is moving towards plastic and flexible displays, compared to conventional glass-based displays: plastic active matrix OLED (AMOLED) panels are much thinner and lighter, enabling either slimmer devices or bigger batteries. Future flexible displays will also make foldable mobile devices a reality. Both Samsung Display and LG Display have recently announced significant investment to expand their production capacity. IDTechEx has upgraded its forecasts and now expects plastic and flexible displays to grow rapidly from a $2bn market this year (2016) to $18bn by 2020.

The rise of plastic and flexible displays will be accompanied by a shift from glass substrates to plastic substrates. However, glass-based displays will remain an important technology, especially in the TV segment where scale-up and cost reduction are still the main challenges.

New applications in wearable devices such as augmented reality (AR) and virtual reality (VR) are also coming to market and provide new

opportunities for suppliers of OLED displays. Sony, Oculus, and HTC have already announced new VR headsets based on AMOLED technologies.

For AR glasses, OLED microdisplays are a major contender against existing LCoS (liquid crystal on silicon) technology.
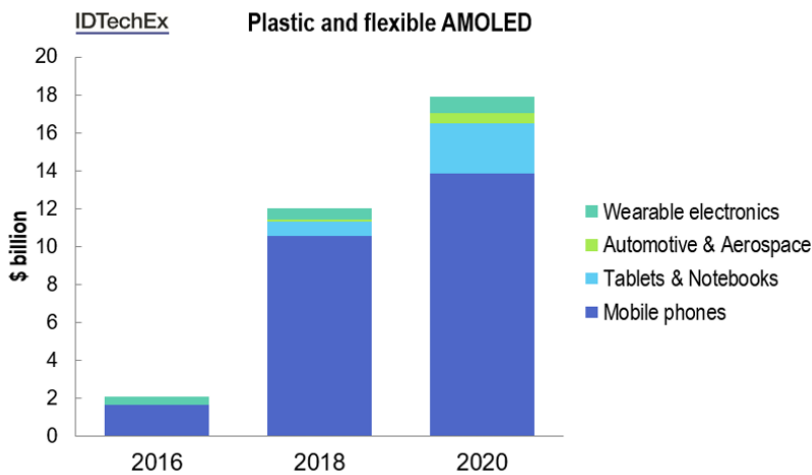
Figure 2 *Plastic and flexible OLED display revenue forecast in four market segment (Source: IDTechEx)*

Beside OLED displays, a very promising field of application is the lighting, in the ever enlarging market of the Solid-State Lighting (SSL) technology, which also include inorganic LEDs and electroluminescent devices.

There are many attractive features of SSL light sources which has placed them as a serious contender in the lighting markets: superior energy efficiency, absence of hazardous metals (mercury free), flexible form factor, high durability and the possibility of intricate light management for energy management and design features. LED-based lighting products have been available for some years now and are the basis for a rapidly growing SSL industry.

OLED technology has been supported through industry-wide projects, especially in Europe, where a large concerted effort has been spent to develop OLED lighting technology. OLED materials and technology development haves been driven by companies and research institutions such as BASF, Merck, Fraunhofer FEP (formerly COMEDD), Novaled, OSRAM, Philips and several universities, to the point where initial OLEDs products for lighting applications are now emerging.

Leading lighting producers such as OSRAM and Philips have introduced limited release commercial products to demonstrate the potential and allow

interested users to try out OLED lighting technology, with other companies such as Black Body, LG, Pioneer, Konica Minolta, etc. also developing products.

In Japan, advanced prototype OLED lighting products have been shown by a number of local companies, while the US Department of Energy has been instrumental in supporting the technology. Recently, OLED lighting products have even become available through mail-order home supply stores in the USA.

	2014-2015	2016-2018	2019-2022	2023-2027
Best efficacies	100 lm/W	130 lm/W	160 lm/W	190 lm/W
First products / prototype	Decorative lighting modules, high price applications B2B	Automotive Lighting, Flexible lighting for high price sector	Specialized building integration, Transparent	Any size, large area free form, 3D
Mass product	-	-	Mass-produced flexible lighting	General and technical building-integrated, flexible, transparent

Figure 3 *Examples of expected OLED lighting applications(Source: OE-A Roadmap for Organic and Printed Electronics)*

OLED lighting products promise novel features in the longer term: large emitting area, diffuse light emission without glare, flexibility and very thin form factors, high efficacy, variable color, and even transparency are just some of the possibilities. New lighting applications can be expected to take advantage of the OLED properties, for example embedded lighting or homogeneous area lighting.

The lighting market is however complex, as it is a highly fragmented space thanks to the existence of a broad technology mix and a diversity of customer needs. The market segments include residential, office, industrial, outdoor, hospitality, museums, shops, automotive, agriculture, and more. Each sector attaches a different degree of importance to upfront cost, energy efficiency, lifetime, light intensity, color warmth and design features. This explains why the technology mix in each sector is different.

IDTecEx assess that the OLED lighting market will grow to 2.2 billion USD in 2026 (optimistic scenario). The market growth will however be very slow until 2019/2020, where the overall sales at panel level will remain below 200 million USD globally. Furthermore, to effectively exploit the properties of the OLED sources, new installations will be necessary, instead to use them as retrofits in existing installations (Figure 4).
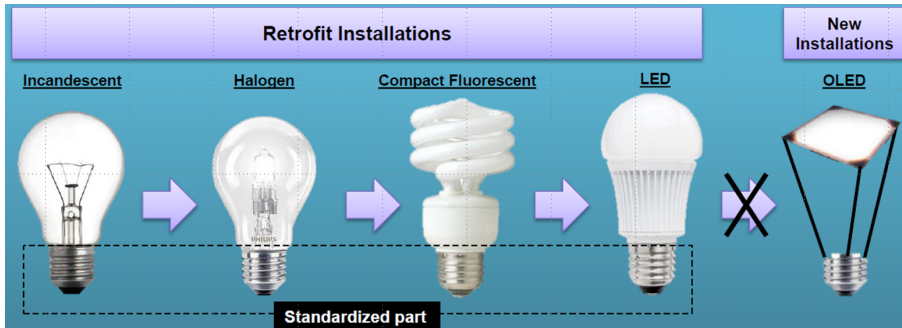
Figure 4 *A new OLED module could not fit any existing lamp, particularly for that based on the classic light bulb*

OLED lighting has the potential to efficiently emit warm light across large surfaces and to bring new and novel form factors into the lighting sector. These are strong selling points on their own, but the challenge is in that they are not always unique. In particular, inorganic LED lighting arrived first onto the market. Its technology, cost structure and supply base have dramatically improved, opening a large performance and cost gap between LEDs and the younger OLEDs. The performance gap has not drastically narrowed despite progress in OLEDs, with companies such as Konica Minolta reporting champion 131 lm/W panels.

The challenge OLEDs are facing is therefore identifying paths for differentiation. The differentiation challenge is also a critical strategy question, because many companies, such as OSRAM and Phillips already have successful and growing businesses in the LED sector.

Surface emission is a possible differentiator, although inorganic LEDs are also able to create effective surface emissions thanks to waveguides, despite they are point light sources. Flexibility is also another way, although OLEDs themselves also face critical technology challenges that stand in the way of them achieving flexibility.

The ability to offer customized or improved design features is also a selling point. In particular, the potential to act at the luminaire level as a slightly modified panel can be a competitive advantage (Figure 5).

Figure 5 *A recent example of an OLED luminaries installation*

From a technological point of view, there are two main approaches to fabricate OLEDs: vacuum deposited small molecule OLEDs and solution processed polymer OLEDs. The former type has been more efficient and therefore the leading technology for lighting. OLED products are currently restricted to rigid glass substrates.

Flexible OLEDs are possible on plastic and metal foils. Furthermore, flexible ultrathin glass appears on the horizon as an attractive substrate. In time, hybrid materials and manufacturing approaches may be used to realize actual OLED lighting products, in order to optimize manufacturing economics.

Current lighting sources present a broad range of competing performance capabilities, and lighting applications are very varied. Competing against existing products will not be made any easier by the prospect that in the short term OLEDs will tend to be non-transparent, small area and on rigid glass substrates. However, already now, OLED benefits can be envisaged, whether due to the novel surface emission for design applications or by virtue of the thinness where space is at a premium.

A number of key parameters for OLED lighting are generally discussed in the industry. The three critical parameters are lifetime, luminance and efficacy. Other important parameters include size, cost and the light quality parameters color rendering index (CRI) and color temperature.

At industry level, parameter definition and reporting standards must be developed, to assure end-users in the lighting industry.

• Lifetime: this refers to T80 (time to 80% initial luminance). A minimum lifetime of 10,000 hours is necessary to support initial applications

in illumination. In the longer term, given the expectations set by LED lighting, 50,000 to 100,000 hours will be required.

• Efficiency: the conversion from electrical energy to light is a critical measure for lighting. 50 lm/W and higher is now available to be competitive and meet new efficient lighting regulations. Lower luminaire losses are to be expected for OLEDs than for other forms of lighting, due to the unique surface emission properties.

• Size: as an area light source, OLED success depends on scalability to large area. Form factors in the range from 10 cm^2 and up to 60 cm^2, either using single devices or arrays of devices, are suitable for lighting products.

• Luminance: area light emitters for ambient or signage lighting are referenced in terms of brightness per unit area (cd/m^2). Low levels in the region of 100-300 cd/m^2 may be sufficient for automotive interiors. High unit lumen output for general lighting will require up to 5,000 cd/m^2, but this will need to be balanced against lifetime.

• Cost: two basic valuations may be considered for OLEDs. For general lighting, OLED light cost needs to be less than 1 euro cent per lumen for mainstream acceptance. However, cost per unit area (for ambient or backlighting) should be in the region of 500-1000 €/m^2.

Core OLED lighting technology has borrowed heavily from OLED display development. There are a number of critical issues related to commercialization: on the one hand, developing components and technologies for outcoupling and encapsulation that are both higher performing and suitable for mass manufacturing is essential for commercial product development. On the other hand, the development of highly efficient and scalable manufacturing processes for reliable and cost effective OLED devices is a must: solutions are in sight, but progress cannot to be taken for granted.

• Encapsulation: the high sensitivity to moisture of OLED materials makes the integrity of current encapsulation methods (glass cap, getter) critical to ensure lifetime performance in the short term. Thin film encapsulation could enable large area, flexibility and integrated in-line production. There are indications that this issue can be tackled in the near future. In order to reduce devices cost and accelerate commercial uptake, the development of new barriers (e.g., inorganic/organic multilayer, laminates) is needed.

• Outcoupling: OLED efficiency can be improved considerably by the use of suitable light extraction and light management techniques, in the form of optical components and structures. Integration into the OLED structure, e.g. in the form of intelligent glass substrates or lenses (microlenses array, pyramids array, prisms foil), index-matched materials and adhesives, that can be introduced into high volume manufacturing processes, is an important area needing further development. Good encapsulation would allow for use

of plastic substrates with better opportunities to achieve improved outcoupling.

• Standardization: Reporting standards need to be established and adhered to (lifetime, structure, improvement factors).

• Manufacturing costs: in view of the current high price of OLED manufacturing and the needed low cost for general lighting, improved manufacturing processes, that enable lower price points and potential for much higher volumes for lighting products, are required. Higher throughput and material utilization efficiency are required from vacuum deposition equipment. Solution processing and printing tooling promises lower cost manufacturing, but needs to be capable of delivering high performance devices. This is becoming the most dominant challenge.

• Investment: moving from R&D and pilot lines to real production is strongly needed to enable broad applications for the OLED lighting technology, but it requires large investments.

In this context lies this thesis.

A particular sector of the lighting is receiving large attention in the last years, the horticultural lighting. In this regard, it is noticeable that in 2016 the Horticultural Lighting Conference was started (http://www.lighting-inspiration.com/event/horticultural-lighting-conference-2016/).

Large area OLED for horticultural application could offer great advantage to the emerging market of LED for horticultural, strongly pushed by OSRAM and Philips (see chapter 3).

1.Organic LEDs

1.1. Functional layers

In principle, an organic light emitting diode consists of a sequence of organic layers between two electrodes, an anode for holes and a cathode for electrons injection, respectively (Figure 6).

Under positive bias, holes are injected from the anode and electrons from the cathode. The charge carriers drift through the layers and meet in the emission layer (EML). Here, they form excitons (neutral excited states) which show a certain probability to decay radiatively (S. Reineke, 2012), allowing the photon emission: this phenomenon is called Electroluminescence (EL).

To achieve highly efficient OLEDs, they have become complex multilayer systems, where each layer has different and specific functionality. Figure 6 illustrates a multilayer OLED sequence with its functional layers. For simplicity, in Figure 6, the highest occupied molecular orbital (HOMO) and lowest unoccupied molecular orbital (LUMO) levels are treated similar to valence and conduction bands in inorganic semiconductors. and the vacuum level is assumed to be aligned. It is worth keep in mind that this is a very rough approximation.
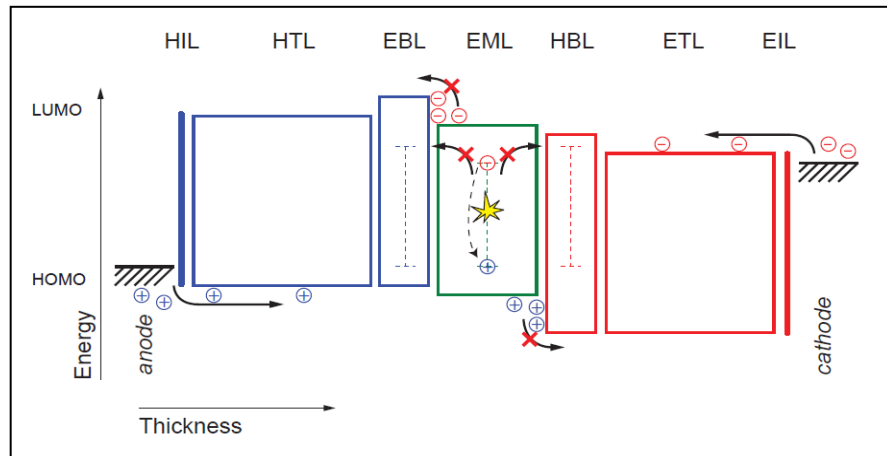
Figure 6*: (color online) Energy diagram of a typical multilayer OLED. Note that in many devices some of the layers depicted are redundant, because different functions may be combined in one layer. From anode to cathode there are: hole injection layer (HIL), hole transport layer (HTL), electron blocking layer (EBL), emission layer (EML), hole blocking layer (HBL), electron transport layer (ETL), and electron injection layer (EIL). Boxes indicate HOMO and LUMO levels of the materials. The dashed lines in the EBL, EML, and HBL are the desired triplet energies of the materials in case of phosphorescent OLEDs.* **(S Reineke, 2013)**.

Holes are injected from a high work function material (the most used, in case of bottom emission OLEDs, is the transparent conductor indium tin oxide (ITO)) into the HOMO level of an organic semiconductor: the hole transport layer (HTL). For an improved injection, a thin hole injection layer (HIL) is used to ease hole injection from the anode into the hole transport layer. This can be achieved by choosing its HOMO level in between the HOMO of the HTL and the ionization potential of the anode Figure 6. A good way to achieve a high performing OLED is to sandwich the EML between the EBL and the hole blocking layer (HBL), in order to confine both the types of carriers as well. The double confinement of the EML keeps spatially separated the excitons from the HTL and ETL, because these layers might be luminescence quenchers or, in case of HTL /ETL materials with a high photoluminescence quantum yield (PLQY), they could act as undesired emission layers, altering the expected device color emission and affecting the whole device efficiency.

1.2. Fluorescent and phosphorescent materials

As mentioned, charges are injected in the EML under the influence of an electric field. At separation of a few nanometers, the Coulombic attraction binds the charges together and they are no longer able to escape one another by thermal diffusion. As a consequence, the total spin of the hole-electron pair can be either S=0 or S=1.

The S=0 is due by the antisymmetric spin interaction of the hole-electron pair and is known as singlet state; instead, the S=1 contains three possible states, all symmetric, and is known as triplet state.

Because the triplet state has a multiplicity of three, on average 75% of the excitons formed are triplet states, with the remaining 25% being singlets.

The spin of the exciton controls its luminescence. Because the emission of a photon conserves spin, quantum-mechanically, only singlet excitons are allowed to decay radiatively. This process is fast (particle lifetimes of ≈ 1 ns), and is known as fluorescence. In contrast, the probability of luminescence from the remaining triplet states is generally so low that almost all their energy is lost to non-radiative processes, with particle lifetimes in the order of 1 ms. This emission from a "disallowed" transition is known as phosphorescence.

The low singlet fraction causes OLEDs based on fluorescent emitter molecules to be rather inefficient, with an upper limit of the internal quantum efficiency of $\eta_{int,fl} = 25\%$, because emission solely occurs in its singlet manifold as shown in Figure 7.

The efficiency of OLEDs can be drastically improved with the introduction of phosphorescent emitting molecules (M.A.Baldo, 1998), (S. Reineke, 2012). It is well known that heavy metal atoms, such as iridium, platinum, palladium, etc., can enhance spin-orbit coupling within a molecule or polymer, weakening the selection rules for previously forbidden transitions (Thompson, 2007), (H. Yersin, 2002), (Yersin, 2004). In these materials, called organometallic complexes, the emission of light is still significantly slower than fluorescence, but the radiative decay rate is faster than the non-radiative one, then the luminescence can be efficient. Simultaneously, the introduction of the heavy metal strongly enhances the intersystem crossing (ISC) rate between singlet and triplet state, with a very high efficiency, close to unity. So, the 25% of singlet excitons are efficiently converted into triplet state, before they can recombine radiatively. Therefore, a phosphorescent OLED material can lead to $\eta_{int,ph} = 100\%$.
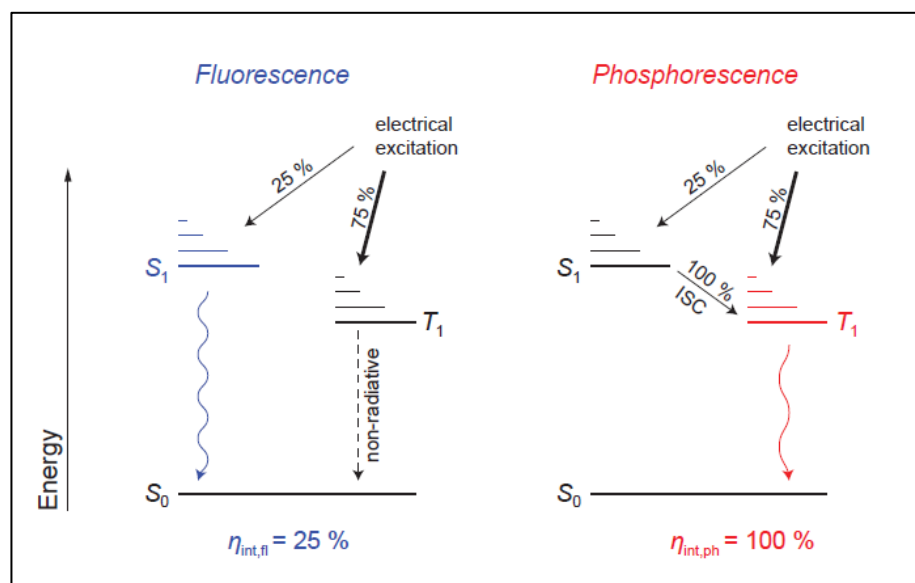
Figure 7: *Population scheme of singlet and triplet level of the organic molecules under electrical excitation. For phosphorescent materials, the singlet excitons created are efficiently transferred to the triplet state via intersystemcrossing (ISC). Additionally, the theoretical limits for the internal quantum efficiency η_{int} are given.*

1.3. Host-guest system

Phosphorescent materials exhibit at least one order of magnitude longer excited state lifetime compared to conventional fluorescence dyes. Then, these excitons are highly exposed to non-radiative "quenching" processes, that limit the device efficiency at high excitation levels, the "efficiency roll-off". A high exciton density increases the probability of the excited state annihilation process, such as triplet-triplet annihilation, triplet-polaron quenching (M. A. Baldo, 2000), (S. Reineke, 2007), and in some case field-induced exciton dissociation. In order to reduce these quenching effects, the phosphorescent material is dispersed into another material (host-material). High quantum yields are typically achieved with a concentration of the phosphor (guest-material) in the host-guest system in the range of 1-10wt%.

In a host-guest system, excitons formed in the host are transferred to the luminescent dye via a combination of Förster and Dexter energy transfer (M. Klessinger, 1995).
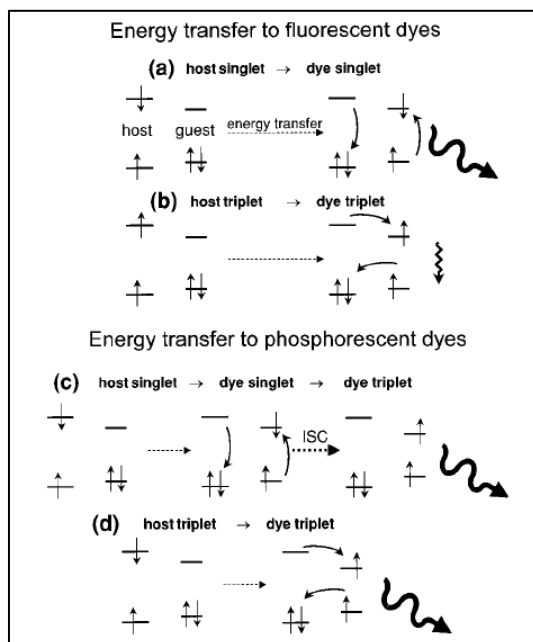
Figure 8 *Proposed energy transfer mechanisms in films doped with a fluorescent dye (a and b), and films doped with a phosphorescent dye. For each molecule, it is shown the ground-state energy level S0, the excited-state singlet level S1 and the excited-state triplet level T1*

Förster transfer is a long range ($\sim40 - 100$ Å), dipole-dipole coupling of donor (D) and acceptor (A) molecules. Since it requires that the transitions from the ground to the excited states be allowed for both D and A species, this mechanism only transfers energy to the singlet state of the acceptor molecule (T. Förster, 1948).

Dexter transfer, instead, is a short range process where excitons diffuse from D to A via intermolecular electron exchange, which required orbital overlap of D and A, resulting in a decrease of this interaction with increasing intermolecular distance (Dexter, 1953). Dexter processes require only that the total spin of the D-A pair be conserved under the Wigner-Witmer selection rules (M. Klessinger, 1995). Consequently, Dexter transfer permits both singlet-to-singlet and triplet-to-triplet transfers.

For a full understanding of all the energy transfers involved in a host-guest system, (M.A. Baldo, 1999) summarizes the energy pathways that could be responsible for the photons emission in a phosphorescent guest and a fluorescent one.

In case of a fluorescent dye, it is shown the singlet-to-singlet transfer Figure 9a),): although both Förster and Dexter processes are capable of singlet-to-singlet energy transfer, Förster mechanism dominates (V. Bulovic, 1998) at low fluorescent dye concentrations because of its long-range nature.

On the other hand, a guest triplet state could be excited at close range by triplet-to-triplet Dexter transfer Figure 9b) Unfortunately, most fluorescent dyes have very short radiative lifetime (~ 10 ns), so at room temperature, phosphorescence is rarely observed and non-radiative losses are dominant. Therefore, the process in Figure 9a) can be considered the responsible for the luminescence in the most fluorescent organic dyes spread in a host material.. Figure 9c) shows singlet-to-triplet transfer between a host and a phosphor: here it is expected that Förster singlet-to-singlet transfer is still the dominant process. Then, thanks to the ISC, with near the unity efficiency, all the singlet excitons are transferred to the triplet ones inside the guest material. Finally, Figure 9d) represents direct Dexter transfer between triplet states of the host and triplet ones of the phosphor dopant.

Let's note that, the host material must be selected carefully with respect to the guest's energy levels. Once the exciton is transferred to the guest sites, it is necessary to confine the exciton on the phosphor so that radiative recombination can occur efficiently (S. Su, 2008), (K. Goushi, 2004). Therefore, the relative position of the host triplet level T_{host} respect to the phosphor triplet state T_{guest} is important. The highest phosphorescence quantum yield of the host-guest system can be expected only for exothermic system, where the triplet level of the host is higher in energy compared to the phosphor ($T_{host} > T_{guest}$). By reducing the energy of the host triplet to a resonant or endothermic system and, hence, allowing back transfer from T_{guest} to T_{host}, the phosphorescent quantum yield of the host-guest system will decrease accordingly, as more excitons remain on the host sites (S.Reineke, 2009).

Finally, another parameter that plays a key role in the working principle of OLEDs is the exciton diffusion. Under electrical excitation, excitons are formed close to an interface between different materials, usually with a generation width below 5 nm (S. Reineke, 2007), thus smaller compared to the total layer thickness (S. Reineke, 2007), (Y.R. Sun, 2006), (J. Wünsche, 2010). Both Förster and Dexter energy transfers do not forbid excitons to migrate throughout organic solids. Here, the net charge carrier is zero, so the only driving force is a gradient in the exciton concentration, leading to a series of uncorrelated hopping steps from molecule to molecule (S Reineke, 2013).

1.4. Hybrid OLEDs and Triplet harvesting

The combination of a fluorescent blue emitter with phosphorescent dyes to form hybrid multicolor OLEDs (i.e. white OLED) is attracting much interest, because it could provide an alternative to use of blue phosphors, which are the current bottleneck in the development of a very efficient white devices.

The reason of these relevant drawbacks are: i) hardly the emission from blue phosphor extends till deep blue region of the visible spectrum, common photoluminescence peak is around 460-470 nm (A. Endo, 2008); ii) blue phosphorescent materials with long term of stability are hard to find (S.Reineke, 2009), (S. Su, 2008); iii) because blue phosphorescent materials need of host materials with even larger bandgap, the operating voltage of devices based on phosphorescent blue emitters will increase (Y. Kawamura, 2005), (N.Seidler, 2010).

In the conventional hybrid architectures, the blue fluorescent emitters used have triplet level T_1 lower than the respective triplet states of the phosphorescent materials. In Figure 9a), it is depicted a possible scheme for the excitation in a conventional hybrid architecture. Here, excitons are created with a fraction q on the fluorescent emitter, leaving 1-q to be generated in the phosphorescent system (green to red). All formed excitons obey the spin statistics presented in the previous section, where the fraction of created singlets is indicated with r_{ST}. Note that in general, r_{ST} may be different for every emitter system (M. Segal, 2003). However, to keep this discussion simple, for r_{ST} it is used the same value for any emitter system here.

Since the triplet level of the fluorescent blue emitter is lower than the respective levels of the phosphorescent materials, efficient transfer from T_1 of the phosphors to that of the blue fluorescent dye can occur, represented by the rate k_{P-F}. The latter triplet level is non-radiative (nr), thus excitons reaching it will be lost for emission, forming a quenching channel for triplet excitons. A way to extinguish this channel is to introduce a thin interlayer between fluorescent and phosphorescent system. The energy transfer leading to a $k_{P-F} > 0$ is Dexter type, requiring orbital overlap, so an interlayer thickness of 2 nm is sufficient (S Reineke, 2013).

In this architecture, another non negligible exciton quenching channel is due to the direct formation of triplet excitons on the fluorescent triplet level, which is proportional to $q*(1 - r_{ST})$. According the theory explained in the section 1.2, *(1 - r_{ST})* is in the order of 75% (triplet states formation rate), the only way to reduce this channel is to reduce q. However, this will decrease the fluorescent intensity at the same time *($q*r_{ST}$)*.
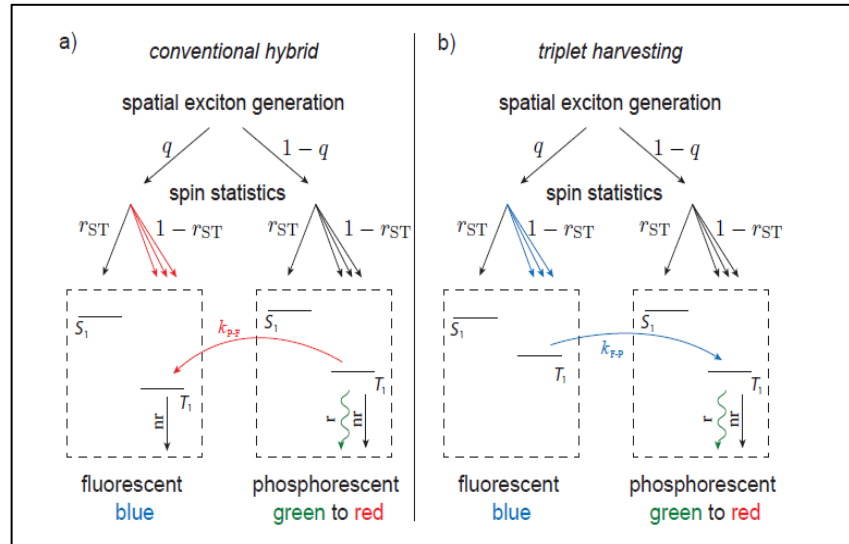
Figure 9: *Scheme for the electrical excitation in a) conventional hybrid and b) triplet harvesting concepts. Here, q denotes the fraction of excitons that are created on the blue fluorophore, r_{ST} is the fraction of singlet excitons formed, `r' and `nr' stand for radiative and non-radiative, respectively, and k_{F-P} and k_{P-F} are the energy transfers from fluorophore to phosphor or vice versa* (S Reineke, 2013).

The only way to reduce the losses leading to the two above explained quenching channel is to use a fluorescent blue material with a T_1 level higher, or at least equal, than the T_1 level of the phosphorescent emitters (Figure 9b). The different relation of the energy levels reverse the direction of the energy transfer, transforming the quenching rate k_{P-F} into an additional path (k_{F-P}) to excite the phosphor triplet levels. If this triplet harvesting mechanism is incorporated inside the device, it allows to reach an internal quantum efficiency of 100%.

The triplet harvesting concept is based on the fact that non-radiative triplets formed in the fluorescent materials can find accessible sites for recombination which are spatially separated and only reached via diffusion. The consequence of the triplet diffusion into the emissive phosphorescent sites is a higher likelihood of the triplet-triplet annihilation, so that the quantum efficiency of the green to red system is strongly reduced as a function of the exciton level, thus current level (roll-off). So, it must be kept in mind that the exciton generation zone it should be such that the average distance a triplet has to travel to reach a phosphor site is as short as possible.

2.Electrical behavior and modeling

2.1. Introduction

So far, it was explained the mechanisms behind of OLEDs operation, from the excitons formation to photons emission. Before forming the excitons, two fundamental steps happen: carriers injection from the metal contacts, and carrier transport in the bulk material. These two processes have impact on the electrical behaviour of an OLED.

The purpose of this chapter is to provide a brief presentation of the scenario regarding transport mechanisms in materials used in the OLED devices. This topic is large and not trivial; for a more complete treatment of this subject, the reader should refer to the specialized papers indicated in the text.

To describe most of the physical mechanism in an organic material is common to use many concepts derived from inorganic semiconductor physics, as it was done for the following physical models shown in this chapter. However, there are some peculiarities and differences of organic semiconductor to their inorganic counterpart.

Since most polymeric and small molecules based materials for OLEDs form disordered amorphous films without a macroscopic crystal lattice, it is not possible to adopt mechanisms developed for molecular crystals.

Because of the absence of extended delocalized states, charge transport is usually not a coherent motion in a well defined bands, but rather a stochastic process of hopping between localized states, which leads to the typically observed low carrier mobility ($\mu \ll 1$ cm^2/V s).

Additionally, many of the materials in OLEDs are wide-gap materials with energy gaps of 2-3 eV, or even more. Therefore, the intrinsic concentration of thermally generated free carrier is generally negligible (<

10^{10} cm^{-3}) and from this point of view these materials can be considered more as insulators than as semiconductors (W. Brütting, 2001).

As explained in the previous chapter, in an OLED there is the necessity to use contacts with different work function (usually high work function as anode, and low work function as cathode) in order to obtain double-carriers injection at the base of the exciton formation. Using contacts with different work function leads to the presence of non-negligible built-in voltage V_{bi} across the organic layers.

Neglecting the energy level shift due to the interface dipoles, the built-in voltage is equal to the contact-potential difference of the two electrodes. So, the physical importance of V_{bi} is that it reduces the applied external voltage V, such that a net drift current in forward is achieved if V exceeds V_{bi}. Thus, in the following equations, there will be the tacit assumption that the affective voltage across the organic layers under forward bias condition is $V = V_{Forward} - V_{bi}$.

2.2. Charge transport in organic material

Only in the very special case of high material purity, low temperature and high crystallinity, organic materials can exhibit band-like transport behavior similar to that one of classic inorganic semiconductor. More often, organic semiconductors show a disordered structure, so the charge carriers move inside them through an intermolecular process of hopping between adjacent molecules.

Furthermore, charge carriers can be localized by defects, disorder or potential wells caused by the polarization. If the lattice is irregular or the carrier becomes localized on a defect site, the lattice vibrations are essential to let the carrier move from one site to another. This is an activated process and the mobility increases with increasing temperature.

FIGURE 3.1
Hopping transport mechanism—if the lattice is irregular, or if the carrier becomes localized on a defect site, then lattice vibrations are essential if the carrier is to move from one site to another. This is an activated process and the mobility increases with increasing temperature.
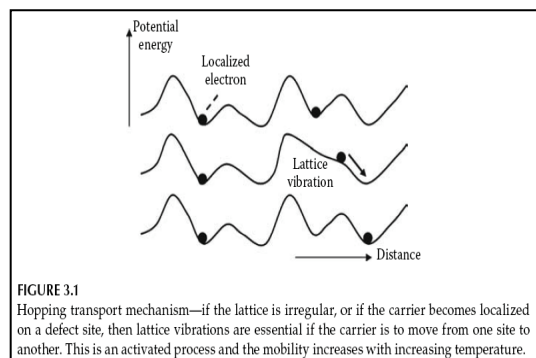
Figure 10 *Hopping transport mechanism*

Independently from the specific mechanism of the charge movement, conduction based on electron movement can be described by the relation $J = -qn_e\mu_e\vec{E}$, where J is the current density, q is the elementary charge, n_e electron density, μ_e electron mobility and is defined as: $\mu_e = \frac{v_d}{\vec{E}}$, and v_d is the drift velocity of the electrons.

The mechanism of the electron movement is hidden within the electron mobility μ_e that represents the relation (ratio) between applied field strength and drift velocity.

Focusing on the most common case of disordered organic materials, two models are here illustrated, applied to describe the hopping conduction mechanism: the Nearest Neighbor Hopping (NNH) and the Variable Range Hopping (VRH). In the former, an electric charge "jumps" from a spatial localized energy level to the nearest neighbor (Figure 11a), while in the latter the charge can jump several levels away from the original one, i.e. variable range (Figure 11b).
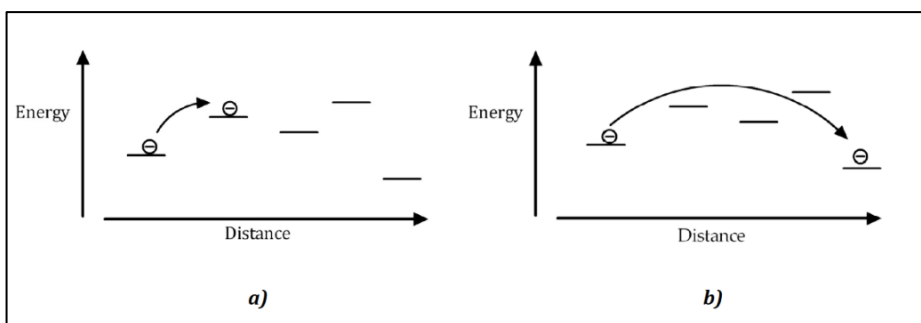
Figure 11 *Hopping conduction: a) nearest neighbor hopping (NNH), b) variable range hopping (VRH).*

The transition probability from one energy level to another is expressed as the product of some terms, taking into account:

- wavefunctions overlapping between states: this term has an exp(-αR) dependence, where α^{-1} is the wave function localization length and R is the distance between initial and final levels;
- Phonons availability: if the initial and final states have energy separation of E, energy conservation rules require a second particle bridging this gap, in order to enable the charge hop. This mechanism is generally fulfilled through molecules vibration, i.e.

> phonons. The term dependence is $\exp(-E/k_B T)$, where k_B is Boltzmann constant and T is temperature;

The probability (*p*) per unit time of a charge jumping between two localized states is therefore proportional to:

Eq 1

$$p \sim \exp(-Q);$$

Eq 2

$$Q = \left(\alpha R + \frac{E}{k_B T} \right);$$

When *E* is smaller than $k_B T$, the αR term dominates, leading to a NNH mechanism; *Q* is minimized for minimum *R*, when the final level is the nearest one. On the other hand, when *T* is low and phonons energy and number are small; $E/k_B T$ cannot be neglected with respect to αR. In this situation, balancing energy and distance, a distant level could possess a smaller *Q* than the nearest neighbour and a VRH regime occurs.

Hypothesizing a casual diffusive mechanism as the driving force of the electron motion, electrical conductivity σ in hopping regime can be calculated as follow:

Eq 3

$$\sigma = q n \mu;$$

Eq 4

$$\mu = \frac{qD}{k_B T};$$

Eq 5

$$D = \frac{1}{6} p R^2;$$

Here, *q* is the electron charge, *n* is the electron density and μ is the charge mobility, determined by the Einstein relation. *D* is the diffusion coefficient, in which hopping probability is taken into account according to NNH

mechanism. On the contrary, in the case of VRH regime, conductivity has the characteristic temperature dependence expression

Eq 6

$$\sigma = \sigma_0 \exp\left(-\frac{T_0}{T}\right)^{\frac{1}{4}};$$

where T_0 and σ_0 are constant given by model parameters (R, α, etc.).

2.3. Charge carrier injection and transport in OLED

There are two limiting regimes of device operation for an OLED, namely space-charge limited current (SCLC) and injection limited current.

- Injection limitation occurs if the injection barrier is so large that injection from the contacts does not provide an inexhaustible carrier reservoir.

Carrier injection into semiconductor is usually treated by Richardson-Schottky (RS) thermionic emission (S.M.Sze, 1981), based on lowering of the image charge potential by the external field $F = V/d$. The current density J_{RS} as a function of the field is given by:

Eq 7

$$J_{RS}(F) = A^* T^2 \exp(-\frac{\Phi_B - \beta_{RS}\sqrt{F}}{K_B T})$$

with the Richardson constant $A^* = 4\pi q m^* k_B^2/h^3$ (= 120 A/cm^{2}K^2) for m* = m$_0$), $\beta_{RS} = \sqrt{(q^3/4\pi\varepsilon\varepsilon_0)}$, Φ_B is the zero-field injection barrier. (q: elementary charge; m_0: free electron mass; k_B: Bolzman's constant; h: Planck's constant; ε relative dielectric constant, ε_0: vacuum permittivity).
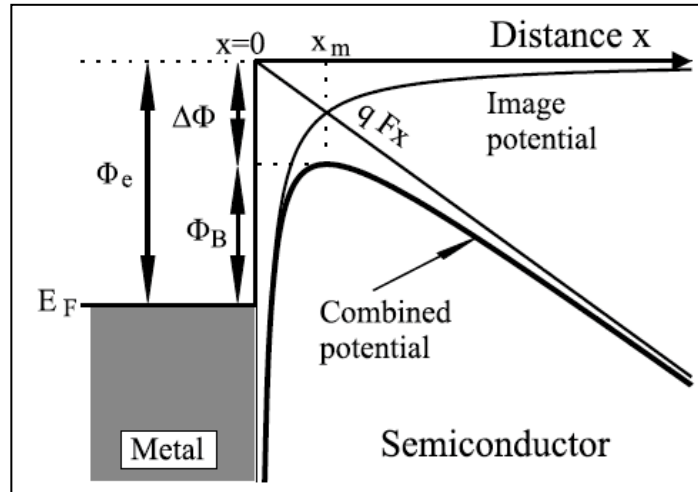
Figure 12 *Schematic of barrier level for Richardson-Schottky (RS) thermionic emission: the electric field lowers the surface barrier by an amount of DΦ, and increases the emission curren..*

Another injection mechanism is the Fowler-Nordheim (FN) tunnelling (Figure 13), where unlike RS emission, Coulombic effect of the image charge is ignored and it is considered only the tunnelling through a triangular barrier into continuum states:

Eq 8

$$J_{FN} = \frac{A^* q^2 F^2}{\Phi_B \chi^2 k_B^2} \exp(-\frac{2\chi \Phi_B^{2/3}}{3qF}),$$

$$\text{with } \chi = \frac{4\pi\sqrt{2m^*}}{h}$$

Electrical behavior and modeling
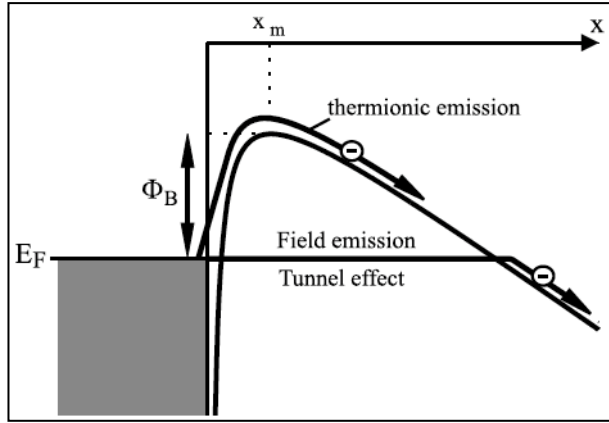
Figure 13 *Schematic of barrier level for Fowler-Nordheim tunnelling*

- SCLC in an OLED can occur if at least one contact is able to inject locally higher carrier densities than the material has in thermal equilibrium without carrier injection. This problem was extensively treated by Lampert and Mark, studying SCLC in insulators (M.A. Lampert, 1970). In case of a perfect insulator, without intrinsic carriers and traps and for a charge carrier mobility independent of the electric field, the SCLC obeys the Mott-Gurney equation (N. F. Mott, 1940):

Eq 9

$$J_{SCLC} = \frac{9}{8}\varepsilon\varepsilon_0\mu\frac{V^2}{d^3}.$$

where d is the device thickness.

In the presence of traps, if they are distributed in energy, they will be gradually filled with increasing electric field, then, the current will increase faster than quadratic until all traps are filled (W. Brütting, 2001).

A fully analytic derivation, in case of trap-charge limited current (TCLC), considering the following trap exponential energy distribution, N_t is the total trap density and a characteristic decay energy E_T:

Eq 10

$$N_T(E) = \left(\frac{N_t}{k_B T}\right)\exp\left(\frac{E - E_{Lumo}}{k_B T}\right)$$

is given by:

15

Eq 11

$$J_{TCLC} = N_{Lumo} \mu q \left(\frac{\varepsilon \varepsilon_0 l}{N_t q (l+1)} \right)^l \left(\frac{2l+1}{l+1} \right)^{l+1} \frac{V^{l+1}}{d^{2l+1}}$$

Where, N_{Lumo} is the density of states in the Lumo band, $l=E_t/k_BT$.

2.4. Mobility contribution

If the assumption of field-independent charge-carrier mobility, so far used, is dropped, an analytic solution in case of absence of trap is still possible.

Using a Poole-Frenkel (PF) field dependence of the mobility, (with β the PF factor, which indicates the strength of the field dependence):

Eq 12

$$\mu(F) = \mu_0 \exp(\beta \sqrt{F})$$.

This field dependence is very frequently observed in amorphous molecular material, doped polymers and also most conjugated polymers (P. M. Borsenberger, 1993).

So, the current density, in case of trap-free SCLC, is a good approximation:

Eq 13

$$J_{SCLC} = \frac{9}{8} \varepsilon \varepsilon_0 \mu_0 \frac{V^2}{d^3} \exp(0.89 \beta \sqrt{F})$$

Note that, apart from the dependence of the current on voltage (then the electric field), the dependence on the thickness of the organic layer provide a unique criterion to distinguish between the underlying mechanism above mentioned. Indeed, it is possible to list the functional dependence of the current on the thickness at constant electric field F for these three situations:

   i. purely injection limited behaviour, the current at constant field has no explicit thickness dependence (Injection limitation occurs if the injection barrier is so large that injection from the contacts does not provide an inexhaustible carrier reservoir.

   Carrier injection into semiconductor is usually treated by Richardson-Schottky (RS) thermionic emission , based on lowering of the image charge potential by the external field $F = V/d$. The current density JRS as a function of the field is given by:

    ii.   Eq **7** and Another injection mechanism is the Fowler-Nordheim (FN) tunnelling (Figure 13), where unlike RS emission, Coulombic effect of the image charge is ignored and it is considered only the tunnelling through a triangular barrier into continuum states:

    iii.   Eq **8**);

$$j = j(F);$$

    iv.   trap-free space-charge limited conduction, with (or without) a field-dependent mobility, the current at constant field scales with d^l (Eq 9, and This field dependence is very frequently observed in amorphous molecular material, doped polymers and also most conjugated polymers .

So, the current density, in case of trap-free SCLC, is a good approximation:

    v.   Eq **13**)

$$j = j(F)/d;$$

    vi.   trap-charge limited conduction, with an exponential trap distribution and field-independent mobility, the current at constant field scales with d^l with $l > 1$ (Eq 11)

$$j = j(F)/d^l;$$

However, the only way to take into account also the trap effect is to carry out some numerical simulations: in this case, the solution will be given only in parametric form.

In the last years, this approach is catching the interest of several research groups. They provide different simulation software, instead of analytic solutions, for most problems in the organic electronic, using a mathematical model for the mobility like PF model, as further constraint in the set of the basic equations that govern the steady state behaviour of these materials.

Unfortunately, PF model does not take into account the disordered nature of the organic materials, nor include the physical process of hopping of the charge carriers within a certain distribution of the energy states. The reason is that, PF model is an empirical model, which has not been derived from a physical point of view.

Recently, thanks to numerical computing, two new mobility models have been developed :the Extended Gaussian Disorder Model (EGDM) and the Extended Correlated Disorder Model (ECDM). The mathematical expressions for both models are based on Monte-Carlo simulations and are too complicated to be given here in their explicit forms, and their treatment is far from the aim of this work.

The main difference to the Poole-Frenkel models is that EGDM and ECDM mobility depends not only on the electric field and the temperature, but also on the charge carrier concentration. This is a consequence of the concept of distributed transport states.

The EGDM has been first introduced by Pasveer et al. (W.F. Pasveer, 2005) and describes the mobility of an organic material within a Gaussian density of states. The consequence is a dependence of the mobility not only on the electric field and the temperature but also on the charge carrier concentration.

The ECDM, has been first published by Bouhassoune et al. (M. Bouhassoune, 2009) and is very similar to the EGDM. The mobility function depends not only on the electrical field and the temperature but also on the charge carrier. However, in contrast to the EGDM, the ECDM assumes a correlated energetic disorder, resulting into a higher dependency on the electric field than the EGDM.

There is evidence that the EGDM is more applicable for the description of polymers, while the ECDM is the better model for small molecules (S.L. M. van Mensfoort, 2010).

These two models are called 2nd generation mobility models and are applicable only for numerical computing, but both of them are a promise for a future and better understanding of the organic matter.

3.Purple OLED for Horticultural Application

3.1. Horticultural applications

light for indoor cultivation has significantly grown, since, it enables intensification of production, improves quality, and allows cultivation wherever natural light is not sufficient (e.g. northern latitudes, indoor cultivation, harsh environments).

Light is one of the most important variables affecting phytochemical concentration in plants (Kopsell, 2008). It has been reported that the use of LED lamps in lettuce cultivation positively affected growth and phytochemical traits (Li, 2009). Other investigations showed the LED-induced increase of the anthocyanins in grapes (Kataoka, 2003) and in lettuce leaves (Tsormpatsidis, 2008), carotenoids in tomato fruits and anthocyanins in tomato leaves (Giliberto, 2005) and vitamin C in lettuce leaves (Ohashi-Kaneko, 2007).

The reasons are basically related to the specific features of the absorption spectrum of the chloroplast pigments.
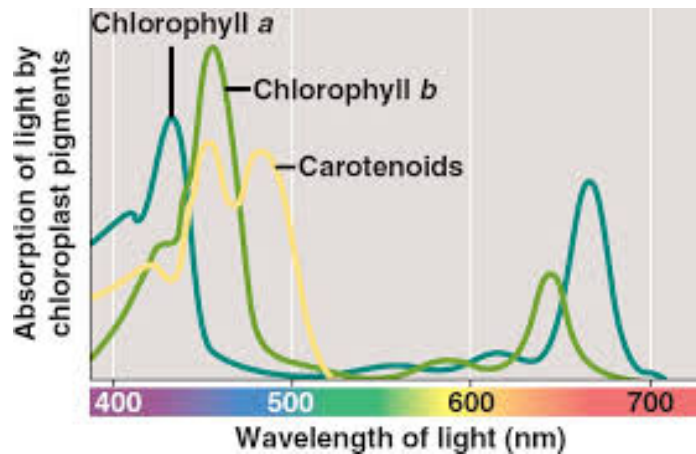
Figure 14: *Plants are able to satisfy their energy requirements by absorbing light from blue and red part of sunlight spectrum.*

Note that both chlorophylls absorb light most strongly in the red and blue portions of the spectrum, Figure 14. Indeed, green light is poorly absorbed, so when white light, which contains the entire visible spectrum, shines on leaves, green rays are transmitted and reflected giving leaves their characteristic green color).

Unfortunately, a more complete understanding of the physiological and phytochemical plant response to the spectral components of light, and fully detecting of the optimal LED light spectra composition (i.e. ratio between red and blue portions of the spectrum or a protocol for the light exposition) is still far for obtaining an horticultural product, and in last years, many efforts have been doing in this direction.

In this contest, OLEDs technology could be a key challenge to achieve these purposes: as the only surface-type light source, OLED lighting offers the best quality light in term of uniformity.

A commercial LED panel needs of a suitable design work (for spatial distributions of red LED arrays and blue ones) according to customer's demand, making absolutely not feasible the manufacturing of a unique product.

Instead, an OLED panel has not only an intrinsic uniformity in term of light's shape, but it can guarantee the same red/blue light ratio onto all its surface.

Furthermore, this technology produces very low heat (<35°C), eliminating the need for heat sinks [ref. http://www.lgoledlight.com], making it very human friendly and preventing any damage due to high temperatures for all plants.

3.2. Proposed Hybrid structure

In this thesis, we propose an approach to fabricate purple light OLEDs.

The way used to obtain a purple color light was to merge the spectral emission from a red phosphorescent dopant Ir(btp)2(acac) (Bis[2-(2'-benzothienyl)pyridinato-N,C3'](acetylacetonato)iridium(III)), with a deep blue fluorescent emission from α-NPD (N,N′-Di(1-naphthyl)-N,N′-diphenyl-(1,1′-biphenyl)-4,4′-diamine). So, the proposed device architecture is a hybrid fluorescent-phosphorescent OLED, where the triplet energy levels of the materials employed (T_1,α-NPD = 2.26 eV, T_1,Ir(btp)2(acac) = 2 eV) (G. Schwartz, 2009), (F. Chen, 2003), allow the triplet harvesting from α-NPD towards Ir(btp)2(acac), as shown in the section .

The purposes of this activity of the PhD work are to demonstrate the feasibility of a hybrid purple OLED using commercial materials, and understand the mechanisms driving its behavior. Therefore, a series of experiments have been set up to optimize the exciton energetic transfers and the color emission of the final device. For these aims, it was not necessary a full optimization of the device, in terms of its efficiency, such as the use of a blue fluorescent material with a higher PLQY (photoluminescence quantum yield) than α-NPD (i.e., PLQY of α-NPD is 42% (H. Mattoussi, 1999) while 4p-NPD shows a PLQY of 94 (G. Schwartz, 2009)), or the use of doped HTL and ETL, or light outcoupling methods.

For the complete list of the materials, (chemical name, molecular structure etc.) exploited in this thesis see

Appendix A2.

In the following sections, the tool used to evaluate the effectiveness of all the energy transfers and the device optimization is the calculation of the number of the emitted photons at a specific wavelength. This calculation is based on the measurement of the absolute light spectral emission $F(\lambda)$ of the devices, which was measured using a spectroradiometer Gooch&Housego OL770 coupled with an integrating sphere. The unit of measurement of $F(\lambda)$ is W/nm (watt per unit wavelength (λ)). The number of the emitted photons can be calculated by dividing $F(\lambda)$ at a specific wavelength by the photon energy hc/λ at that wavelength, where h is the Planck's constant, and c is the velocity of the light.

Obviously, the total number of the emitted photons can be calculated by integrating $F(\lambda)/(hc/\lambda)$, over λ along the range of the emitted wavelengths. This procedure is quite similar to that one used to estimate the external quantum efficiency (EQE) (I. Tanaka, 2004), which is another parameter for the OLEDs characterization.

3.3. Blue emission optimization from α-NPD

As explained in the chapter 1, the phosphorescent emitting materials need to be dispersed at low concentration as dopants in a host material. Different host materials were suitable for the red dopant to be used in this work. But, with the aim to optimize the interface α-NPD÷host-guest system and reach a proper alignment of the energy levels to exploit, at the best, the α-NPD fluorescence, two different host materials were tested: SimCP (9,9'-(5-(Triphenylsilyl)-1,3-phenylene)bis(9H-carbazole)) and CBP (4,4′-Bis(9-carbazolyl)-1,1′-biphenyl).

In Figure 15, the normalized (respect to the red peaks at 620 nm) spectral emissions of two purple OLEDs are shown. These devices have similar architectures and the same red dopant concentrations in the two hosts:

- Dev A: ITO (170 nm)/ PEDOT:PSS (30 nm)/ α-NPD (60 nm)/ SimCp:Ir(btp)2(acac) (2%wt) (25 nm)/ BCP (9 nm)/ Alq3 (10 nm)/ Ca (20 nm)/ Al (80 nm);

- Dev B: ITO (170 nm)/ PEDOT:PSS (30 nm)/ α-NPD (60 nm)/ CBP:Ir(btp)2(acac) (2%wt) (25 nm)/ BCP (9 nm)/ Alq3 (10 nm)/ Ca (20 nm)/ Al (80 nm).
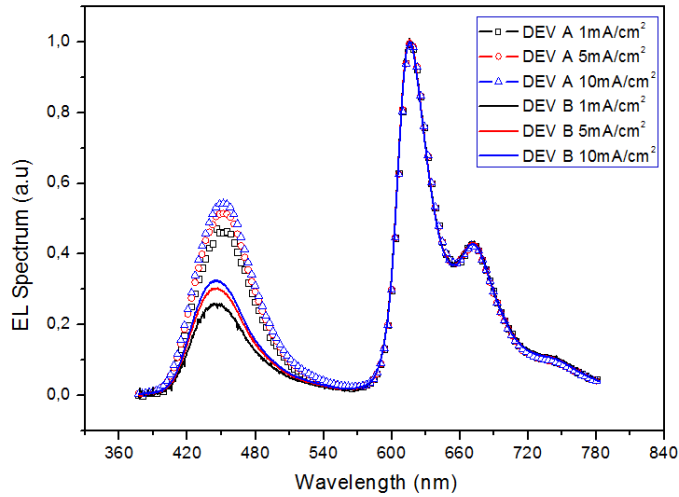
Figure 15 *(Symbols) Spectra at different current density for a device with SimCp as host material (DEV A). (Lines) Spectra at different current density for a device with CBP as host material. All spectra are normalized respect to the red peaks at 620 nm.*

It is clear that the blue peak at 443 nm in the DEV A is higher than the one of the DEV B. The reason of this stronger blue emission is due to a better alignment between LUMO levels of SimCP (2.56 eV) and α-NPD (2.4 eV), respect to CBP (2.7 eV) and α-NPD (see Figure 16).
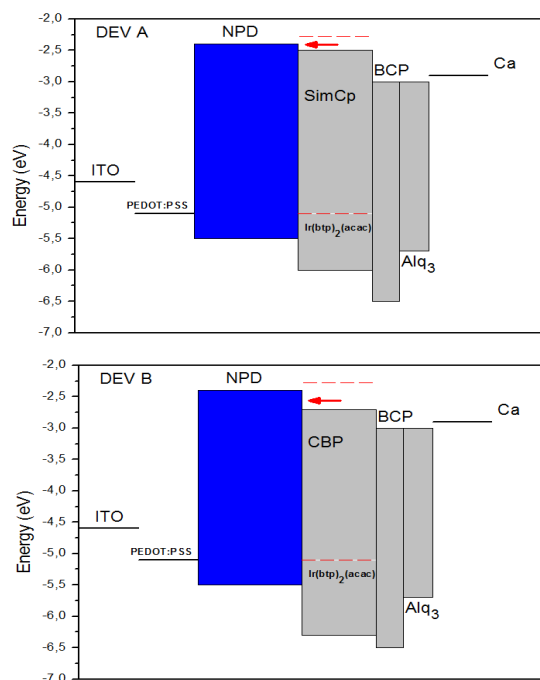
Figure 16: *Energy diagrams for DEV A and DEV B. (Red dashed lines) HOMO and LUMO of red dopant: Ir(btp)2(acac). The red arrow highlight the reduced step for the electrons to "jump" in the LUMO level of α-NPD in case of DEV A.*

The lower energy barrier at the interface α-NPD÷SimCP promotes the excitons generation and the consequent fluorescent emission in the α-NPD, because more electrons can pass into this material from the SimCP.

The proof of a lower energy barrier for the injection of the electrons is given in Figure 17, where the electron currents of two electron-only devices are depicted; the two devices are:

- DEV C: ITO (170 nm)/ BCP (20 nm)/ NPD (60 nm)/ SimCP (50 nm)/ Ca (20 nm)/ Al (80 nm);
- DEV D: ITO (170 nm)/ BCP (20 nm)/ NPD (60 nm)/ CBP (50 nm)/ Ca (20 nm)/ Al (80 nm).

See Figure 18 for the related energy level diagram.
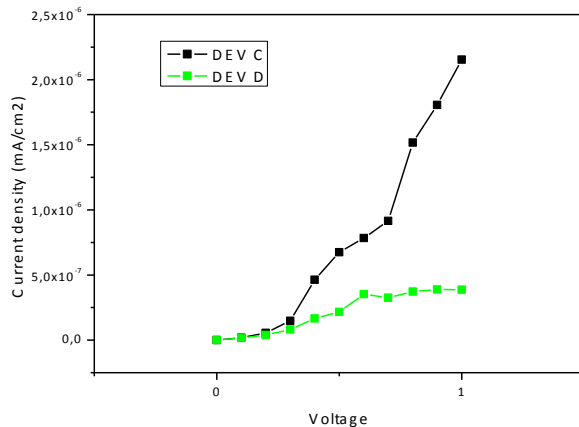
Figure 17: *Current density of DEV C and DEV D. The fast increase of the current in DEV C is the proof of an easier electron transport using SimCP instead of CBP at the interface with α-NPD.*

In these devices, a hole blocking material (BCP) is used to avoid the holes injection from the ITO into the NPD. In Figure 18, the higher current of DEV C is due to the more effectiveness of the electron injection at the interface NPD÷SimCP. In DEV D, the larger barrier at the interface NPD÷CBP can be crossed by electrons only applying high voltages, which could even be catastrophic for the devices, and surely not optimal for their efficiency. For this reason, the current-voltage measurements are taken up to 1 V as voltage polarization.
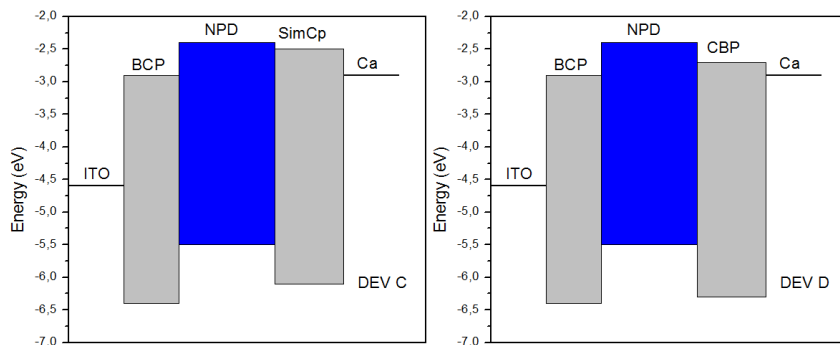
Figure 18: *Energy diagrams for the electron-only devices: DEV C and DEB D. A deep HOMO level of the BCP near the ITO avoids the holes injection in the devices.*

25

The luminous flux of the devices is proportional to the rate of the radiative exciton recombination, hence to the rate of recombination of the minority charge carriers in the α-NPD. Since the α-NPD is close to the anode contact, and the holes mobility in the α-NPD is larger than the electrons mobility, it can be claimed that, at the interface α-NPD÷SimCp, the minority charge carriers are the electrons.

Defining $n(x)$ as the electrons concentration in the α-NPD layer, where x is the distance inside the α-NPD from the interface α-NPD÷SimCp, where the electrons are injected, and $\tau_n(x)$ the mean lifetime of the electrons (Figure 19).
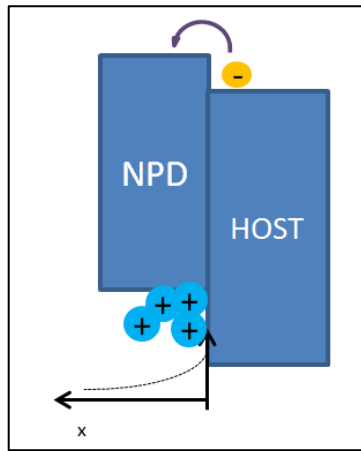
Figure 19: *At the interface α-NPD÷SimCp electrons jump into LUMO energy level of the α-NPD. Here, electrons are the minority charge carriers, so the excitons formation depends on the electrons recombination.*

According to the Shockley-Read-Hall recombination statistics in steady state, the position-dependent recombination rate of the electrons in the α-NPD, $r(x)$, is then given by:

Eq 14

$$r(x) = \frac{n(x)}{\tau_n(x)}$$

Combining the steady-state continuity equation for the electrons in the α-NPD and the electrons current density formulation:

Eq 15

$$\begin{cases} \dfrac{\partial n}{\partial t} = \dfrac{1}{q} \nabla \cdot \vec{J}_n(x) - \dfrac{n(x)}{\tau_n(x)} \\ \vec{J}_n(x) = qD_n \nabla n(x) + q\mu_n n(x) F(x) \end{cases}$$

where $F(x)$ is the position-dependent electric field.
It is possible to demonstrate (see Appendix), that $r(x)$ is :

$$\frac{n(x)}{\tau_n(x)} = \frac{n(l)}{\tau_n(l)} \exp\left(\frac{x-l}{L}\right)$$

where L is the characteristic electron decay length $L = \mu_n \tau_n(l) F(0)$ and l is the thickness of the α-NPD layer.
The total recombination rate per unit area is then:
Eq 16

$$R = \int_0^l r(x)dx = \frac{n(l)}{\tau_n(l)} L\left[1 - \exp\left(\frac{-l}{L}\right)\right]$$

Taking into account the following two observations: i) in a fluorescent material, only 25% ($\eta_{int,fl} = 25\%$) of the excitons can decay radiatively (see section 1.2), ii) it was demonstrated that, without any precaution, in a standard OLED architecture, about the 80% of the generated photons are trapped inside the device (S Reineke, 2013), it can be concluded that the product among $\eta_{int,fl}$, the outcoupling efficiency (20%), and R, gives an estimation of the total number of photons, per second and per unit area, emitted by an OLED (P.E. Burrows, 1996).

Because $\eta_{int,fl}$ is imposed by the quantum mechanics, and assuming to not introduce mechanisms to reduce the light trapping (or, conversely, to not increase the light outcoupling), we can operate only on R to act on the device behavior. In particular, the expression of R was used to optimize the thickness "l" of the α-NPD layer. The best value of l is such that the exponential in R is negligible, however l cannot be too large, in order to not reduce too much the electric field across the α-NPD (in the equation of L, this means a reduction of $F(0)$) and not increase the series resistance of the device because of a large thickness of the NPD layer. Therefore, a good choice for an optimum value of l is 4-5 times the decay length L.

For this issue, the luminescence of blue OLEDs exploiting α-NPD as the emitting material, with different thicknesses l, was studied. In order to optimize the value of l and, at the same time, taking into account the effect of the interface α-NPD÷SimCp used for a purple OLED, the architecture

under investigation was: ITO (170 nm)/ PEDOT:PSS (30 nm)/ NPD (l)/ SimCP (25 nm)/ BCP (9 nm)/ Alq3 (10 nm)/ Ca (20 nm)/ Al (80 nm).

The values of l initially tested were: 8 nm, 35 nm, 60 nm and 100 nm. For each type of devices, the total number of the emitted photons per second was evaluated, as explained in the previous section, then, dividing by the emission area (7 mm^2), by $\eta_{int,fl}$ and by the outcoupling efficiency, a total recombination exciton rate R was calculated.
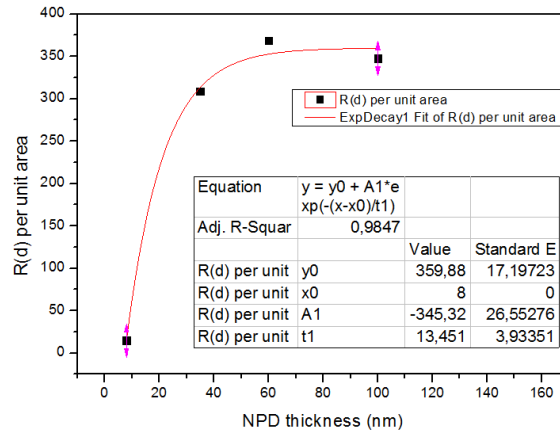
Figure 20: *(Black Squares) R values for devices with different thickness of α-NPD (l); (Red Line) fitting curve, using an exponential equation. All the devices were driven at same current supply of 1 mA.*

.

In Figure 20, a fitting curve based on an exponential function, like that in the expression of R where L is the characteristic electron decay length $L = \mu n \tau n(l) F(0)$ and l is the thickness of the α-NPD layer.

The total recombination rate per unit area is then:

Eq 16, was plotted. From this, the fitting parameter t_1, corresponding to L in the expression of R, was extracted.

The extrapolated value of L is 13.45 nm, leading to an optimum value for $l \approx 60$ nm, choosing it as 4.5 times the decay length L, which assures that the 98.9% of the exponential in the equation of R is extinguished.

In Figure 21, the R values for devices with a larger and smaller thickness of α-NPD are plotted. As expected, further increment of l leads to a reduction of the electric field across the α-NPD, resulting in a lower value of R. Whereas, thin values of l (2 nm, 4 nm up to 8 nm) represent a lower limit to the validity of this model. The reason could be: in a thin layer, a strong molecular disorder and non-negligible interface effects tend to inhibit good bulk conduction or, at least, provide alternative transport mechanisms in comparison with those dominating in thicker layers. Indeed, as it was explained in the chapter 2, the dependence of the current on the thickness, at constant electric field, identifies the mechanism behind the conduction type.
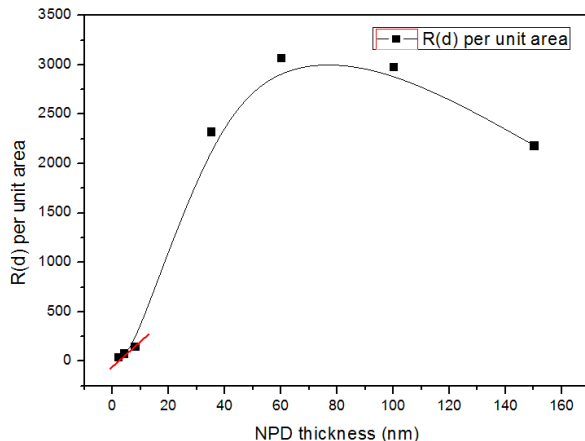
Figure 21: *(Black Squares) R values for devices with a larger range of l (2 nm, 4 nm, 8 nm, 35 nm, 60 nm, 100 nm, 150 nm). The red line points up the behavior of R in a very thin layer of α-NPD.*

3.4. Triplet Harvesting in red phosphorous.

So far, it was demonstrated how a blue emission occurs in this hybrid architecture; namely, a proper alignment between LUMO levels of SimCP and α-NPD allows a direct injection of the electrons in the α-NPD layer which implies its fluorescence.

Instead, the red emission is due to the excitons forming in the host material, which main recombination zone is close to the interface SimCP/BCP, because the main accumulation zones are due to the deep HOMO level of BCP for holes and the low LUMO of SimCP for electrons (see energy diagram of DEV B in Figure 16). The excitons, forming in the SImCP layer, lead to the red emission according to all host-guest mechanisms explained in the section 1.3.

One of the advantages of this architecture is the triplet harvesting in the α-NPD for red emission, that takes place at the interface α-NPD/SimCP÷Ir(btp)2(acac).

Indeed, in addition to the two above mechanisms for the emission, according to the proposed energy transfer, an additional path (k_{F-P}) is allowed to excite the red phosphor triplet levels (Figure 22).

29
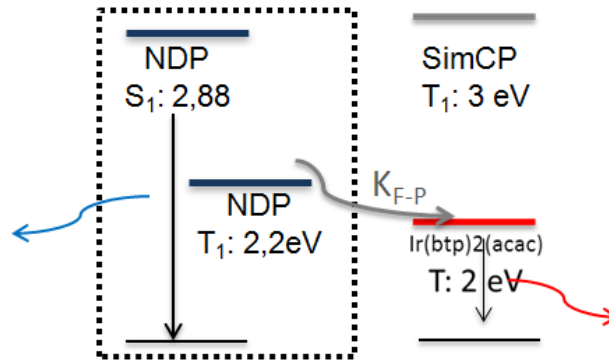
Figure 22: *Proposed energy transfer in the purple architecture. Additional path (k_{F-P}), to excite the phosphor (Ir(btp)2(acac) triplet levels, allows to reach an internal quantum efficiency of 100%.*

The effect of the triplet harvesting can be seen in Figure 23. It shows the number of the photons, due to the red peak normalized to that of the blue peak, in a set of samples with different intrinsic SimCP layer thickness from 0 to 8 nm between α-NPD and SimCP÷Ir(btp)2(acac).

Without intrinsic SimCP (0 nm), the device has a conventional number of red photons compared to blue ones. With increasing intrinsic SimCP layer thickness, the red intensity decreases, that means k_{F-P} contribution is no longer substantial.

So, the monotonous decreasing behavior of the curves in Figure 23 and the emission spectra, normalized to the blue peak plotted in Figure 24, confirm the harvest of triplet excitons from the α-NPD into the red phosphor.

The photons ratio depicted in Figure 23 exhibits a notable decreasing in the devices with 5 nm onwards, while it is more constant within 2 nm of SimCP, as much as the current increases.

A way to better understand what happens to the excitons, when an intrinsic SimCP layer thickness of 2 nm is placed at the interface α-NPD/SimCP÷Ir(btp)2(acac), it could be to analyze the absolute number of red and blue photons related to the device without intrinsic SimCP.
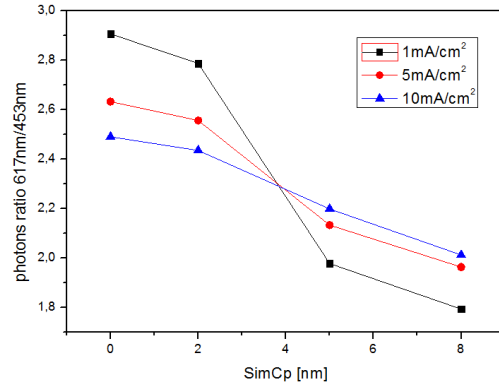
Figure 23: *Number of the red photons (617nm) normalized to blue photons (453nm). The structure of the devices is: ITO (170 nm)/ PEDOT:PSS (30 nm)/ NPD (60 nm)/ SimCP (d)/ SimCP÷Ir(btp)2(acac) (2%wt) (25nm)/ BCP (9 nm)/ Alq3 (10 nm)/ Ca (20 nm)/ Al (80 nm). The thickness d of the the intrinsic SimCP tested is: 0 nm, 2 nm, 5 nm, 8 nm.*
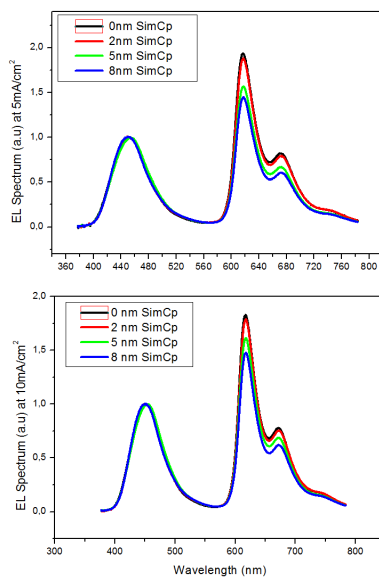
Figure 24: *Spectra of the purple devices at different thickness of intrinsic SimCp (above spectra are taken at 5 mA/cm^2 as current supply, the below ones are taken at 10 mA/cm^2).*

31
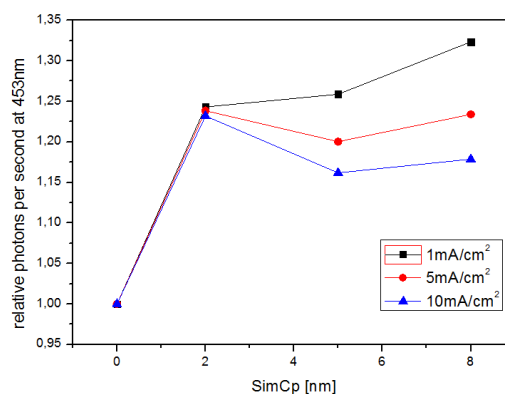
Figure 25: *Singlet to Singlet Förster transfer is allowed at 0 nm of SimCp. Introducing an intrinsic layer of SimCp gives an increment of about 25% of the number of the blue photons, and it is still high as the intrinsic layer thickness increases, demonstrating that after 2 nm Förster transfer is negligible..*
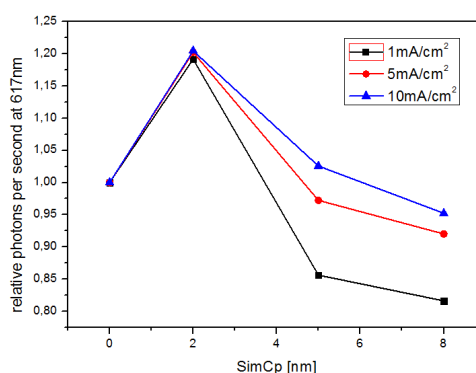
Figure 26: *A premature triplet-triplet quenching occurs even at low current density. 2 nm of intrinsic SimCp reduces this effect. A further increment of the distance between triplet red phosphor and triplet α-NPD resulting in the extinction of the k_{F-P} path.*

From Figure 25 and Figure 26, it is possible to extrapolate two information about the proposed architecture: i) the highest number of red photons occurs at 2 nm of intrinsic SimCp, and for higher thickness this number decreases, as further confirmation of the triplet harvesting above shown; ii) to move the blue emission zone far from the red one enhances the blue content of the light.

These two considerations suggest that there are other energy transfer mechanisms that require to be taken into account.

In the energy transfer model proposed in Figure 22, the orbital overlap between triplet levels of SimCP and α-NPD is not inhibited, allowing an

exothermic energy transfer (k_{P-F}) from SimCP to α-NPD. Here, the triplet level is non-radiative, therefore it does not contribute to the blue emission. The main effect of a quenching channel rate $k_{P-F} > 0$ is, above all, to reduce the direct formation of triplet excitons in the SimCp:Ir(btp)2(acac) layer, resulting in a direct reduction of the emitted red photons. Nevertheless, being this quenching channel an energy transfer triplet-to-triplet, Dexter type, it can be forbidden by using an interlayer material (see section 1.4) with a thickness of 2 nm.

Hence, the reason why the proposed hybrid structure exhibits the highest number of photons for the red peak using 2 nm of intrinsic SimCP is due to a better confinement of the excitons onto the SimCP triplet level, before they are transferred to the red phosphorous according to the host-guest energy transfer rules.

Typically, in a phosphorescent material for OLEDs, the singlet-triplet splitting $Δ_{EST}$ is between 0.5 eV and 1 eV (T. Chen, 2015), which implies, according to the proposed energy model, the singlet energy level of the used red dopant has a deep energy level likely close to the singlet level of α-NPD. Therefore, it is not excluded a singlet to singlet Förster transfer, between α-NPD and Ir(btp)2(acac), implying a reduction of the singlet excitons available for the blue emission. A Förster radius for α-NPD it was estimated around 2 nm (R. R Lunt, 2009), that is experimentally confirmed by the curves in Figure 25. Indeed, as the intrinsic SimCP layer of 2 nm is inserted, an increment of about 25% of the number of the blue photons is reached, and the quantity of the blue photons is still high as this thickness increases, demonstrating that for thickness over 2 nm this Förster transfer is negligible.

A possible explanation for the higher number of red photons reached with 2 nm of SimCp, (it was expected that the maximum there would be with no intrinsic layer of SimCp), it could be that due to the additional path k_{F-P} for the triplet excitons in the red phosphor, even at low current density, the likelihood of the triplet-triplet quenching is increased (see caption 1.3).

For all these observations, it is possible to assert that the best for the proposed hybrid structure is to insert 2 nm of intrinsic layer of SimCP at the interface α-NPD/SimCP÷Ir(btp)2(acac). This expedient allows a total harvesting of the excitons, while reduces enough the premature quenching, as it is further confirmed by the EQE diagram at different current density plotted versus the intrinsic SimCP layer thickness in Figure 27.
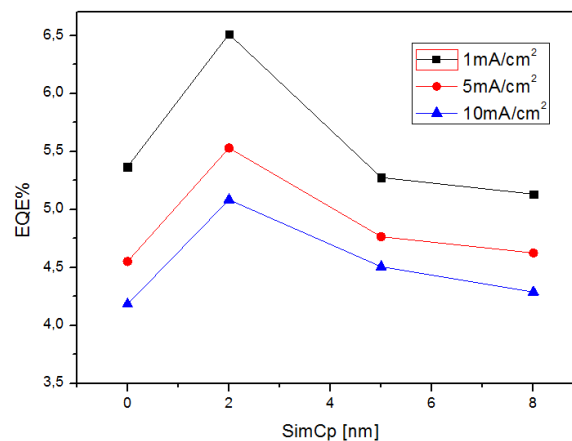
Figure 27: *External quantum efficiency (EQE) of devices under investigation.*

3.5. Large area Purple OLED

Finally, a large area purple OLED was fabricated, by using all the achieved results in the previous studies.

The final structure implemented is: ITO (170 nm)/ PEDOT:PSS (30 nm)/ TcTa (10 nm)/ NPD (60 nm)/ SimCP (2 nm)/ SimCP÷Ir(btp)2(acac) (2%wt) (25 nm)/ BCP (9 nm)/ Alq3 (10 nm)/ Ca (20 nm)/ Al (100 nm)/Ag (100 nm), see Figure 28 and Figure 29, where a purple OLED with an active area of about 50 cm^2 is shown.

Here, a thin layer of TcTa (tris(4-carbazoyl-9-ylphenyl)amine) is used above the hole injection layer (PEDOT:PSS), to further confine the electrons and the excitons (energy LUMO level of TcTa is 2.3 eV, instead HOMO level is 5.7 eV, while its triplet energy level is 2.8 eV (S. Reineke, 2009), ensuring a barrier high enough for all the excitons in the α-NPD).
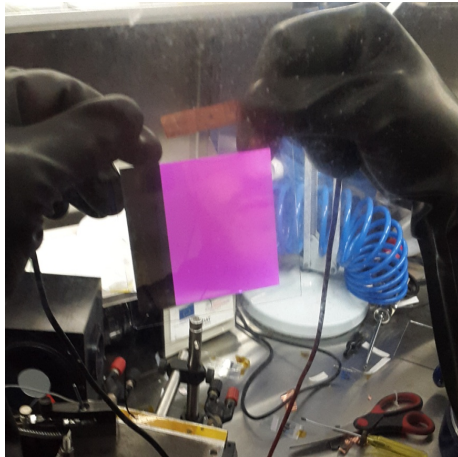
Figure 28: *Purple OLED with active area of ≈ 50cm² (7cm x 7cm). Picture was taken at 6 V as voltage supply.*

Figure 29: *Picture was taken at 7 V as voltage supply. Here, the high brightness has saturated the camera, making light as like a white emission.*

The devices here discussed were not encapsulated, so they never left the glove box, where an inert environmental is kept, with oxygen and water vapor content both less than 1 ppm. Due to a not easy handling, to better evaluate the optical results of the proposed new structure, a small version of the purple OLEDs, with an active area of 1 cm², in Figure 28 and Figure 29 was realized.

In Figure 30 and Figure 31 they are depicted, respectively, the spectra of the emission and the CIE coordinates of the purple devices with an active area of 1cm². Figure 30 proves that spectral emission is stable with current changing: the ratio between red and blue content is kept almost the same, as it is further demonstrated by the CIE diagram in Figure 31, where all points are very close each other (see Table 1).
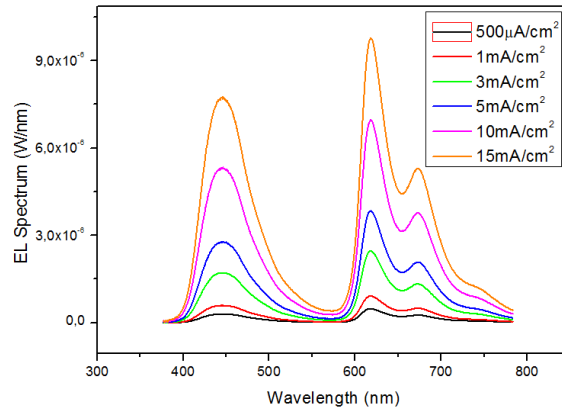
Figure 30: *Absolute spectral emission of the purple OLED of 1cm2 at different current supply.*
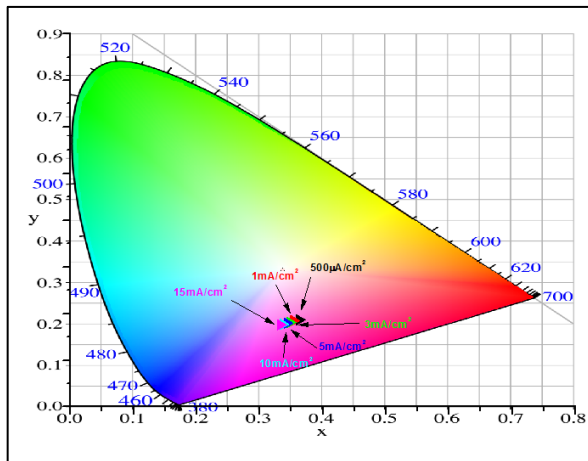
Figure 31: *The CIE (Commission Internationale de l'Éclairge) 1931 coordinates of the device considered in Figure 30.*

All measurements are plotted in reference to the current density, so it is highly likely that at the same current density the large purple OLED exhibits the same optical features.

Table 1 *The CIE coordinates are the numerical description of the chromatic response of an observer to a light source.*

Current density	X	y
$500\mu A/cm^2$	0,3622	0,1866
$1mA/cm^2$	0,3537	0,1846
$3mA/cm^2$	0,3475	0,181
$5mA/cm^2$	0,3431	0,1792
$10mA/cm^2$	0,3365	0,1769
$15mA/cm^2$	0,3325	0,1755

3.6. Conclusion

Light is one of the most important variables affecting plant metabolism.

Due to a specific profile of absorption by chloroplast pigments, only red and blue region of solar light spectrum is exploit, so the use of a combination of red and blue light sources to achieve an overall purple emission, in a way to enhance the plat growing, is currently very attractive.

In this field, OLED technology could offer a solution to overcome some drawbacks relating with the use of LED panels, offering a better quality of the light in terms of uniformity, low working temperature and easily tunable light sources.

In this thesis, OLED purple light was obtained using an hybrid architecture, in which blue component is given out by a very common fluorescent blue emitting material, α-NPD, while red contribution was given by a red phosphorescent material (Iridium based, Ir(btp)2(acac)) in a host-guest system.

At first, the blue emission was maximized, finding the best alignment of the energy levels between α-NPD and the close host material, assuring a good injection of the electrons in the former material. A theoretical model, concerning the excitons distribution in the fluorescent layer, was proposed and used to tune the thickness of this layer, leading to an optimum thickness of 60 nm of α-NPD to allows the maximum of the blue emission.

Then, it was given the proof that, this particular hybrid architecture allows an internal quantum efficiency of 100%, taking advantage of a proper energy coupling between α-NPD and Ir(btp)2(acac), making the former a provider of triplet excitons for the red dopant, otherwise not used in the α-NPD.

As a tool to demonstrate the effectiveness of the energy transfers, the calculation of the number of the emitted photons at a specific wavelength was used.

Furthermore, studying the number of photons that are given out by purple OLED, it has revealed that to have a maximum of the red emission and in general of the EQE, it is fundamental to place 2 nm of intrinsic layer of SimCp, the host material used in this device, next to the α-NPD.

Finally, a large purple OLED with an active area of about 50 cm^2 was made, demonstrating that as soon as an efficient OLED encapsulation system will be available, this device is ready for the experimentation in the a real indoor horticultural cultivation.

4.Metal grid for Large Area OLED

4.1. Large Area OLED

Large area organic light emitting diodes (OLEDs) are becoming very attractive for the next generation of lighting applications.

In a white OLED for lighting, the color point of the emitted light is strictly dependent by and variable with the current supply (Figure 32).

Unfortunately, the limited conductivity of the transparent anode leads to a lateral voltage drop along the contact, which is related to the current flow in the devices.

The most commonly used transparent conductor for OLEDs is the indium tin oxide (ITO). Although ITO has excellent transmittance (about 90% at 550 nm), the value of its sheet resistance (about 10 $\Omega/\square$ for a thickness of 170 nm), it's too high for large area devices, because it induces an inhomogeneous luminance distribution already in devices of a few centimeters of dimensions.
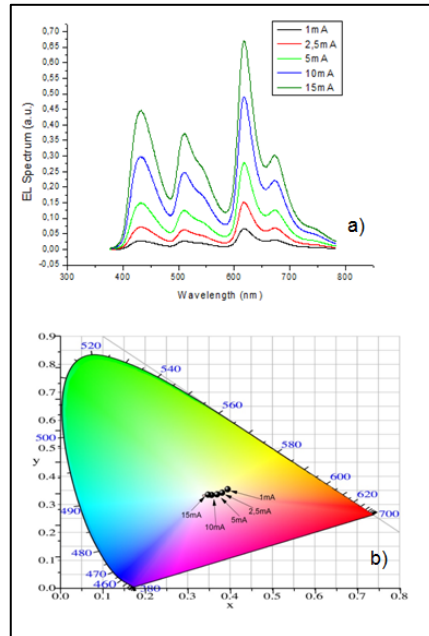
Figure 32: *a) EL Spectrum of White OLED at different current supply. b) CIE (Commission Internationale de l'Éclairge) 1931 color space.*

This aspect is not negligible for a large area white OLED, as it can be easily seen in Figure 32.

A simply way to overcome the low conductivity of the ITO, without replacing it, and keeping a good transparency, is to fabricate a metal grid on the ITO surface.

In this chapter, a mathematical model is introduced to describe the sheet resistance of a hexagonal metal grid on ITO, as a function of geometrical parameters.

The purpose of this work is to present a simple instrument to characterize a metal grid layer, which can be used as a tool to improve the spatial luminance distribution of large area OLEDs enhancing the conductivity of the ITO.

4.2. Theory

For a simple electrical modelling of an OLED with a metal grid, that was first reported by (K. Neyts, 2006), it is possible to consider three conductive layers (Figure 33:): a metallic grid, a transparent bottom electrode (ITO), and a reflective metallic top electrode. In this section, let's call d_b and d_g, and

σ_b and σ_g, respectively, the thickness and the conductivity of the ITO and of the metal grid.
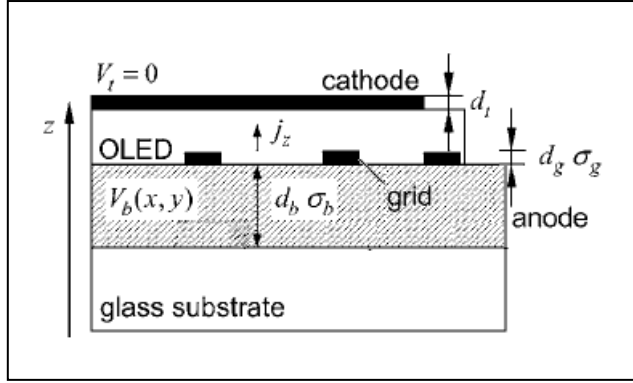
Figure 33: *Cross-section of OLED device with metal cathode and transparent bottom electrode with metal grid.*

Bearing in mind that the thicknesses of these layers (order of 100 nm) are much smaller than the lateral dimensions of the OLED device (> 100 µm), some approximations can be done: i) the cathode can be considered as a perfect conductor and it is grounded, $V = 0$; ii) the organic layers have a much higher resistivity than the bottom electrode, therefore the potential in the bottom electrode is independent of the z-coordinate $V_b(x,y)$; iii) for the same reason, the grid electrode potential is equal to the bottom electrode potential, $V_g(x,y) = V_b(x, y)$; iv) the current density (A/m^2) in the emitting layer is, in first approximation, homogeneous and perpendicular to the substrate, j_z (K. Neyts, 2006).

Now, the lateral current density in the conducting layers (metal grid and ITO) is proportional with the electric field and the material conductivity, for this reason it is possible to discern:

Eq 17

$$\vec{j}_b = -\sigma_b \nabla V_b;$$

Eq 18

$$\vec{j}_g = -\sigma_g \nabla V_g.$$

Applying the conservation of current flux in a stationary situation:

41

Eq 19

$$\nabla \cdot (d_b \vec{j}_b + d_g \vec{j}_g) = -j_z \text{ or } \nabla \cdot (d_b \vec{j}_b) = -j_z ,$$

for regions with or without the presence of the metal grid, respectively.

Eliminating the current densities j_b and j_z, from Eq 17 and Eq **18**, in Eq **19**, leads to the following differential equations for the electrode voltages in the region with and without the metal grid:

Eq 20

$$\nabla^2 V_b = \frac{R_b R_g}{R_b + R_g} j_z \approx R_g J_z \text{ or } \nabla^2 V_b = R_b J_b .$$

Then, $R_{b,g} = 1/(\sigma_{b,g} d_{b,g})$ is the sheet resistance of the electrode.

So, it is possible to model the combination of the bottom electrode with the metal grid as a single electrode with a spatial inhomogeneous sheet resistance $R_{s,tot}$, which corresponds to R_g or R_b in presence of absence of the metal grid, respectively:

Eq 21

$$\nabla^2 V_a(x,y) = R_{s,tot} J_z(x,y)$$

Moreover, OLED luminance (*L*) is proportional with the current, which means, supposing as first approximation that the efficiency η *(cd/A)* is constant,

Eq 22

$$L(x,y) = \eta J_z(x,y) \Rightarrow L(x,y) = \eta \frac{\nabla^2 V_a(x,y)}{R_{s,tot}}$$

The last equation underlines how fundamental is to have, as much as possible, a homogeneous spatial distribution for the anode potential, in order to reach a homogeneous luminance.

4.3. Fabrication of metal grids

As the transparent electrode has been used commercial ITO, sputtered on glass substrates (Delta Technologies, Ltd. on Corning® Eagle XG®). The substrates were cleaned with deionized water and detergent in an ultrasonic bath, then rinsed with acetone and isopropyl alcohol, and dried in oven at 130°C for at least two hours.

All the metals grid were made by lift-off technique, where a sacrificial photoresist is used to create a new layer with the desired pattern (Figure 34).
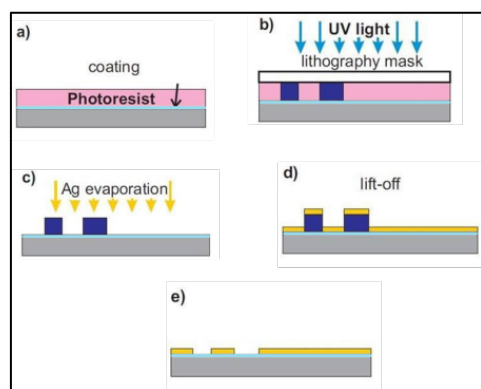
Figure 34: *Lift-off process used for the preparation of the metal grids. a) Deposition of the sacrificial photoresist; b) creation of the inverse pattern on the sacrificial layer (UV Exposure/Etching); c) metal evaporation; d) washing out the photoresist together with the metal in excess on its surface; e) resulting metal pattern.*

The sacrificial layer of the photoresist was spin coated over the substrate. A pattern generator (Heidelberg Instruments) was used to stamp the pattern of the metal grid on the photoresist, than a develop solution was used to remove the exposed areas of the photoresist. In the deposition system (Kurt J. Lesker Company® SPECTROS 150), metal was thermally evaporated at base pressure lower than 5×10^{-7} mbar, on the whole substrate. The sacrificial photoresist was washed out in an acetone bath together with metal on it, in this way only the metal in direct contact with the underlying ITO remains on the substrate.

The geometric shape of the grids under study is the hexagonal one. A hexagonal grid, or honeycomb, is the best way to divide a surface into regions of equal area with the minimum total perimeter (Hales, 2001), and this is a good precondition to achieve the best 2D voltage homogeneity along the anode. In fact, as reported in literature, the voltage loss of others shape grids (i.e. square) is larger than loss in a hexagonal element (K. Neyts, 2008).

Various types of hexagonal metal grids were initially made: different for metal and hexagonal dimensions. The lateral dimension *l* of the hexagons

43

(Figure 35) was: 1 mm, 2 mm, 4 mm and 8 mm. Instead, two metals were exploited: silver, with thickness 20 nm, and aluminum with thickness 80 nm. All grids have the same line width of 150 μm (*W*).

The electrical sheet resistances of the metal grids on ITO were measured by a Four point Probe (NAPSON RESISTAGE RG-80). The optical transmittance measurements were performed using an UV/visible spectrometer (Perkin-Elmer Lambda 900) in the wavelength range from 400 nm to 800 nm. The width and thickness of the metal lines were measured using an optical profilometer (Taylor Hobson® Talysurf CCI).

4.4. Proposed Model.

According to literature (D. S. Ghosh, 2010), (J. H. Park, 2014), to predict the sheet resistance ($R_{s,tot}$) and the transmittance *(T_{tot})* of a combination between a metal grid and an ITO layer, the following equations can be used:

Eq 23

$$T_{Tot} = T_{ITO} \cdot (1 - FF)$$

Eq 24

$$R_{s,tot} = \xi \frac{\rho_G}{\tau_G \cdot FF},$$

Where:

Eq 25

$$FF = \frac{l^2 - (l - p)^2}{l^2}$$

ξ is a correction factor depending on deposition conditions and it is determinate experimentally for a given process; ρ_G and τ_G are respectively the resistivity and thickness of metal; T_{ITO} is the transmittance of the ITO. FF is the filling factor defined by Eq 25, which quantifies the area covered by the metal compared to ITO substrate. Where *l* is the hexagons side length, *p* is the distance between two vertices of the hexagon (the inner one and the outer one), see Figure 35 .
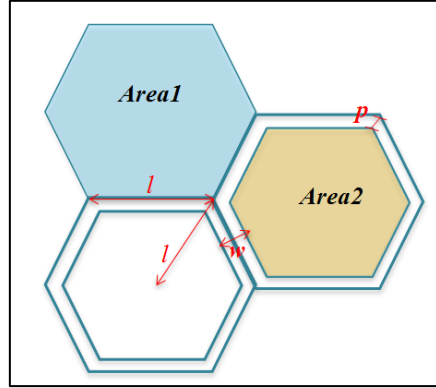
Figure 35: *Filling Factor (FF) quantifies the area covered by the metal, namely, it is the relationship between the external area of the hexagon and the internal one: (Area$_1$-Area$_2$)/Area$_1$.*

The experimental measurements of T_{tot} are in very good agreement with the predictions of Eq 23 (see Table 2). Note that, both experimental and calculated data from Eq 23 for T_{tot} have the same values for both the prepared metal grids. Indeed, in the Eq 23 it is implicit the assumption that the metal is enough thick to be opaque, so the transmittance feature of these anodes depend only on the geometric parameters and not on the metal and thickness used for the grid.

Table 2 *Transmittance (550nm) : same values for both kind of metals*

l [mm]	T_{tot} average [%]	T_{tot} calculated [%]
1	79	75
2	84	82
4	*87*	*86*
8	89	88

The definition here presented of $R_{s,tot}$ (Eq 24) was used in several works in which the anode was made by a metal grid only (Y. Jang, 2013), (J. H. Park, 2014). However, this approach was carried out by Ghosh et al. also in presence of an underlying conducting material, as in this work.

But, comparing the anodes made in this thesis with the ones by Ghosh et al, it appears that neglecting the electrical contribution, in the $R_{s,tot}$ expression, of the underlying ITO, as they did, gives incorrect values.

Indeed, the sheet resistance of the bare ITO is about 12 +/- 2 Ω/□, which is of the same order of magnitude of the data of the $R_{s,tot}$ measured here (see Figure 36), therefore ITO contribution is essential for the electrical behavior of the anodes and cannot be dropped for a right comprehension of the observed data.

Furthermore, considering the expression of $R_{s,tot}$ presented so far, for each process of fabrication, for a given metal and a filling factor, the only degree of freedom, to match the experimental data with the calculated ones through the model, is ξ.

A way to predict $R_{s,tot}$ for new different metal grids is to extrapolate ξ from these first experimental data, using a linear fit of the measured sheet resistances as a function of 1/FF (according to Eq 24).

However, a linear fit was not able to replicate, at best, the measured data. In fact, as it is possible to see in Figure 36, the linear fit equation has an intercept value different from 0, suggesting that these experimental data require an additive term in the Eq 24 to better fit them.

Equation	y = a + b*x	
Adj. R-Square	0,72483	
	Value	Standard Error
R_Al Intercept	4,98717	0,48004
R_Al Slope	0,14169	0,02586
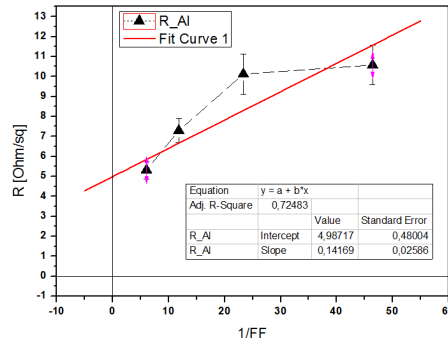
Figure 36: *(black triangles) Measured sheet resistances for the metal grids made of Aluminium. (red line) Fitting curve using a linear fit equation. It is evident how a linear fit doesn't follow these data.*

Furthermore, according Eq 24 and Eq 25, as soon as *l* increases, *FF* tends to zero, and the value of $R_{s,tot}$ to infinite, and this makes no physical sense, because the upper limit of $R_{s,tot}$ should be the sheet resistance of the ITO.

Instead, the model is in a good agreement with the data in the lower limit of $R_{s,tot}$. In fact, in the limit case in which the line width of the metal is equal to its length (*l = p*), which means to have an hexagon full of metal, *FF* assumes the value 1, and the expression of $R_{s,tot}$ becomes the sheet resistance of the metal, and ξ takes into account the effect of the deposition process on the real metal resistivity.

In order to better predict $R_{s,tot}$ value as a function of physical and geometrical grid parameters, it has been developed an extended version of the model, giving to the Eq 24 a second degree of freedom.

First of all, the Eq 25 is rewritten as:

Eq 26

$$1 - \frac{(l-p)^2}{l^2} = 1 - f_F$$

Moreover, to make easier the mathematical manipulation, it was decided to refer to the sheet conductance, defined as the reciprocal of the sheet resistance, so the Eq 24 becomes:

Eq 27

$$G_{s,tot} = \frac{\sigma_G \tau_G}{\xi}(1 - f_F)$$

As established beforehand, introducing a second degree of freedom to consider the electrical influence of the underlying ITO, the expression of $G_{s,tot}$ can become:

Eq 28

$$G_{s,tot} = \sigma_G \tau_G \left[\frac{1}{\xi_1} - \frac{f_F}{\xi_2} \right].$$

It follows that the new expression for $R_{s,tot}$ is:

Eq 29

$$R_{s,tot} = \frac{\rho_G}{\tau_G \left[\dfrac{1}{\xi_1} - \dfrac{f_F}{\xi_2} \right]}.$$

Now, Figure 37 proves that the best fit of the sheet conductance of the actual metal grids on ITO (Figure 37 a) silver grids, Figure 37 b) aluminum grids), as a function of f_F is a straight line corresponding to the Eq 28.
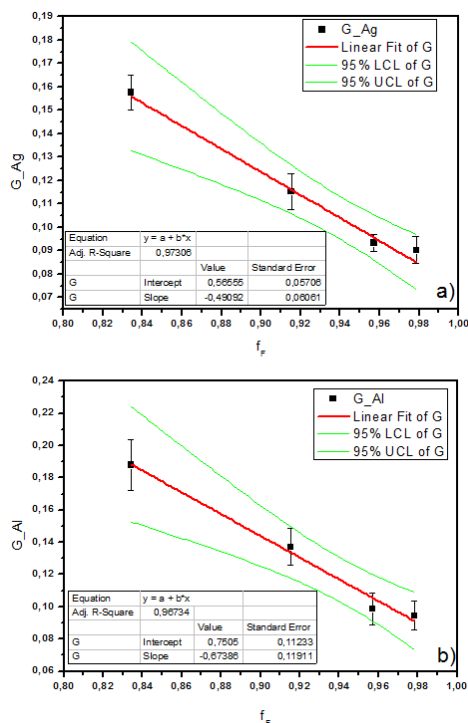
Figure 37: *(black squares) Sheet Conductance of the grids as a function of f_F of the experimental data. (red lines) Linear fit according to* Eq 28. *(green curves) Upper and lower limits of the 95% confidence interval of the mean value. Values related to silver grids a), and aluminium b).*

This approach leads to a good linear regression and, as it is possible to verify in Table 3, all the calculated values for the sheet resistances, using ξ_1 and ξ_2 extrapolated by the fit in Figure 37, are in very good agreement with the experimental data.

Table 3

l [mm]	R_s average (silver grids) [$\Omega/\square$]	R_s calculated (ξ_1 =2.23; ξ_2=2.57) [$\Omega/\square$]	R_s average (Aluminum grids) [$\Omega/\square$]	R_s calculated (ξ_1 =6.06; ξ_2=6.71) [$\Omega/\square$]
1	6.3±0.3	6.4 ±0.5	5.3 ±0.4	5.3 ±0.8
2	8.6 ±0.6	8.6 ±0.7	7.3 ±0.6	7.5 ±1

| 4 | 10.7 ±0.4 | 10.4 ±0.8 | 10.1 ±0.9 | 9.5 ±1 |
| 8 | 11.1 ±0.7 | 11.7 ±0.9 | 10.5 ±2 | 10.9 ±2 |

4.5. Physical meaning of the model

When the lateral dimension l of the hexagons increases, in the extreme case it tends to infinite. This means, from the mathematical point of view, that f_F tends to the unity, and the Eq 29 for the sheet resistance becomes:

Eq 30

$$R_{s,tot} = \frac{\rho_G}{\tau_G \left[\dfrac{1}{\xi_1} - \dfrac{1}{\xi_2} \right]}$$

The physical point of view suggests that the hexagons are so large, that only the underlying ITO gives a contribution to the conduction, so there is no metal grid. Therefore, from Eq 30, it is deduced that ξ_1 and ξ_2 are the parameters, which somehow connect the ITO sheet resistance with the resistivity and the thickness of the used metal.

Effectively, using ξ_1 and ξ_2, extrapolated by the fit for both metals, in the Eq 30, not only it gives almost the same values in the two cases, but also these values correspond to the measured sheet resistance of the ITO (see Table 4), confirming the physical role of linking ξ_1 and ξ_2 with the metal parameters.

Table 4

ITO R_s estimated from Ag [$\Omega/\square$]	ITO R_s estimated from Al [$\Omega/\square$]	ITO R_s measured [$\Omega/\square$]
13.3 ±1	13.1 ±2	12.0 ±0.3

Drawing conclusions: the most established models to characterize the sheet resistance of a metal grid take into account the conductivity of the metal layer only (D. S. Ghosh, 2010), (Y. Jang, 2013). Instead, the proposed model has an extended validity, considering in a such way also the electrical influence of the transparent layer of ITO.

49

4.6. Rs -T plot

The electrical and optical performances of metal grids made in this work are summarized in the Rs -T plot, in Figure 38.

Obviously, the best grid should present high transmittance and low sheet resistance, which means the symbols in Figure 38 should be located in the upper left corner of the diagram. Unfortunately, both bare ITO and all metal grids made so far, are in the right side of the diagram (red and black squares in Figure 38).

Now the question is: which parameter is it necessary to change, in order to move the metal grid position toward the left side of the diagram?

An answer could be offered by the model above presented. Indeed, using Eq 29 with extrapolated ξ_1 and ξ_2, it is possible to predict what would be the position in the R_s-T plot for a metal grid with a different filling factor f_F, in other words with different geometrical dimensions (side l and metal width W), and different metal thickness.
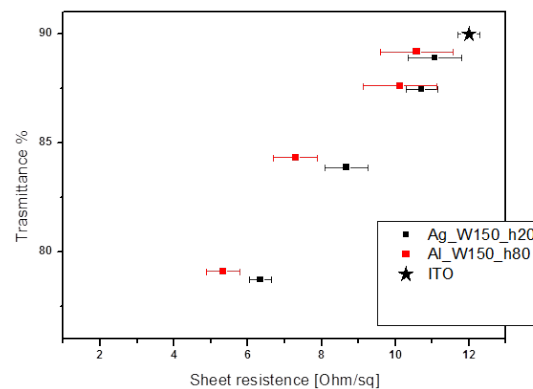

Figure 38: *(Red and Black squares) Transmittance plotted vs. the sheet resistance of the prepared metal grids on ITO. (Black star) Position on the R_s-T plot of the bare ITO. In the legend: h20 means a metal thickness of 20 nm for the silver grids, and h80 means a thickness of 80 nm for the aluminium grids.In the legend: h20 means a metal thickness of 20nm for the silver grids, instead h80 means a thickness of 80nm for the aluminium grids.*

It is clear in Figure 39 that, the fundamental parameter that allows to move from the right side to the left side of the graph is the metal thickness (green diamonds in Figure 39).

Decreasing the metal width increases the transmittance, but has a negligible effect on the sheet resistance (blue diamonds in figure). Indeed, as

further demonstrated by red diamonds in Figure 39, which corresponds to the R_s-T plot of metal grids with reduced width, but with 80 nm of metal thickness instead of 20 nm, they have roughly the same position of the green diamonds, which correspond to metal grids with same thickness but larger metal width.

In conclusion, for a fixed filling factor and hence transparency, an increase in the metal thickness reduces dramatically the sheet resistance.
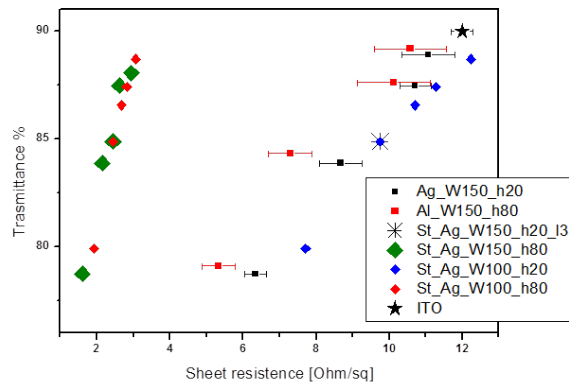

Figure 39: *(Diamonds) Predicted R_s-T position using Eq 29. Except for the red squares, all values are referred to silver grids. (Black asterisk) R_s-T position for a silver grid with hexagon side length of 3 mm, metal width of 150 microns and metal thinness of 20 nm.*

4.7. Conclusions

The relatively high sheet resistance of the most used conductive transparent material, the ITO, used as anode in the bottom emitting OLED configurations, introduces a drop voltage over the anode, leading to an inhomogeneous luminance distribution of the devices area, that takes place as soon as the dimensions of the OLEDs increase above a few centimeters. This point is the main obstacle to achieve high uniform large OLEDs.

A way to overcome it, without replace the ITO and keeping a good transparency, is to fabricate a metal grid on the ITO surface.

To this purpose, in this work, a study of hexagonal metal grids on ITO was made. In particular, it was demonstrated that conduction of hexagonal metal grids coupled with ITO layers can be well described using, for the first time here, a linear model with two degree of freedom, to include the ITO contribution to the overall conduction.

Using together this model and the R_s-T (sheet resistance vs. transmittance) plot, it is possible to design and fabricate transparent anodes

for large area OLEDs with a good trade-off between conduction and transparency.

Bibliography

A. Endo, e. a., 2008. Measurement of photoluminiscence efficiency of Ir(III) phenylpyridine derivates in solution and solid-states films. *Chemical Physics Letters,* Volume 460, pp. 155-157.

C. W. Tang, S. V., 1987. Organic electroluminescent diodes. *Appl. Phys. Lett,* 51(913).

D. S. Ghosh, T. L. C. a. V. P., 2010. High figure-of-merit ultrathin metal transparent electrodes incorporating. *APPLIED PHYSICS LETTERS ,* Volume 96, pp. 041109-1-3.

Dexter, D. L., 1953. A Theory of sensitized Luminescence in Solids. *Journal of Chemical Physics ,* 21(5), pp. 836-850.

F. Chen, S. C. G. H. S. P. Y. Y. M. K. J. K., 2003. Energy transfer and triplet exciton Confinement in Polymeric Electrophosphorescent Devices. *Journal of Polymer Science: Part B: Polymer Physics,* Volume 41, pp. 2681-2690.

G. Schwartz, S. R. T. C. R. K. W. a. K. L., 2009. Triplet Harvesting in Hybrid White Organic Light-Emitting Diodes\. *advanced -functional Materials,* Volume 19, pp. 1319-1333.

Giliberto, L. P. G. P. P. W. J. F. P. B. P. F. A. M. G. G., 2005. Manipulation of blue light photoreceptorcryptochrome 2 in tomato affects vegetative development, flowering time, andfruit antioxidant content.. *Plant Physiol ,* Volume 137, p. 199–208..

H. Mattoussi, H. M. C. M. Y. L. J.-. K. Z. H. K., 1999. Photoluminescence quantum yield of pure and molecularly doped organic solid films. *Journal of applied Physics,* Volume 86, p. 2642.

H. Yersin, D. W. H. J. S. R. S. a. M. G., 2002. Orhanometallic Pt(II) Compounds. A Complementary Study of Triplet Emitter Based on Optical High-Resolution and Optically Detected Magnetic Resonance Spectroscopy. *Inorganic Chemistry,* 41(19), pp. 4915-4922.

Hales, T.-., 2001. The Honeycomb Conjecture. *Discrete Comput Geom.*

Bibliography

I. Tanaka, S. T., 2004. Precise Measurement of External Quantum Efficiency of Organic Light-Emitting Devices. *Japanese Journal of Applied Physics,* 43(11A), p. 7733–7736.

J. H. Park, D. Y. L. Y. K. J. K. K. J. H. L. J. H. P. T. L. a. J. H. C., 2014. Flexible and Transparent Metallic Grid Electrodes Prepared by Evaporative Assembly. *Applied Materials & Interfaces.*

J. Wünsche, s. r. B. L. a. K. L., 2010. Measurement of triplet exciton diffusio in organic light-emitting diodes. *Physical Review B,* Volume 81, p. 245201.

K. Goushi, R. K. J. B. H. A. C. A., 2004. Detecting luminiscence from triplet states of organic semiconductors at room temperatures using delayed electroluminescence spectroscopy. *Applied Physics Letters,* Volume 95, p. 7798.

K. Neyts, A. R. M. M. S. M. a. J. B., 2008. Conductor grid optimization for luminance loss reduction in organic light. *JOURNAL OF APPLIED PHYSICS ,* Volume 103.

K. Neyts, M. M. A. U. N. A. E. W. L. K. F. Q. H. K. W. K. L., 2006. Inhomogeneous luminance in organic light emitting diodes related to electrode resistivity. *JOURNAL OF APPLIED PHYSICS ,* Volume 100, p. 114513.

Kataoka, I. S. A. B. K., 2003. Role of ultraviolet radiation inaccumulation of anthocyanin in berries of 'Gros Colman' grapes (Vitis ViniferaL.).. *J. Jpn. Soc. Hortic. Sci.,* Volume 72, pp. 1-6.

Kopsell, D. K. D., 2008. Genetic and environmental factors affecting plantlutein/zeaxantin.. *Agro Food Ind. Hi-Tech ,* Volume 19, pp. 44-46.

Li, Q. K. C., 2009. Effects of supplemental light quality on growth andphytochemicals of baby leaf lettuce.. *Environ. Exp. Bot.,* Volume 67, p. 59–64.

M. A. Baldo, C. A. a. S. F., 2000. Transient analysys of organic electrophosphorescence. II Transient analysis of triplet-triplet annihilation. *Physical Review B ,* Volume 62, p. 10967.

M. Bouhassoune, e. a., 2009. Carrier-densty and field-dependent charge- carrier mobility in organic semiconductors with correlated Gaussian disorder.. *Organic Electronics,* 10(3), pp. 437-445.

M. Klessinger, a. J. M., 1995. *Excited States and Photo-Chemistry of Organic Molecules.* New York: VHC Publishers .

54

Bibliography

M. Segal, M. A. B. R. J. H. S. R. F. a. Z. G. S., 2003. Excitonic singlet-triplet ratios in molecular and polymeric organic materials. *Physical Review B,* Volume 68.

M.a Baldo, D. F. O. Y. Y. A. S. S. S. M. T. a. S. F., 1998. Highly efficient phosporescent emission from organic electroluminescent devices. *Nature,* Volume 395, pp. 151-154.

M.A. Baldo, D. F. O. M. E. T. S. R. F., 1999. Excitonic singlet-triplet ratio in a semiconducting organic thin film. *Physical Review B,* 60(20), pp. 14422-14428.

M.A. Lampert, a. P. M., 1970. *Current Injection in Solids.* New York: Academic.

M.A.Baldo, d. F. O. Y. Y. A. S. S. S. M. T. a. S. F., 1998. High Efficient Phosphorescent emision from organic electroluminescent devices. *Nature,* Volume 395, pp. 151-154.

N. F. Mott, R. G., 1940. *Electronic Process in Ionic Crystals.* Oxford: Clarendon.

N.Seidler, S. R. K. W. B. L. A. T. J. V. G. a. K. L., 2010. Influence of the hole blocking layer on blue phosphorescent organic light-emitting devices using 3.6-di(9-carbazolyl)-9-(2-ethylhexlyl)carbazole as host material. *Appllied Physics Letters ,* 96(9).

Ohashi-Kaneko, K. T. M. K. N. F. K., 2007. Effect of light quality ongrowth and vegetable quality in leaf lettuce, spinach and komatsuna.. *Environ.Control Biol.,* Volume 45, p. 189–198.

P. M. Borsenberger, D. S. W., 1993. *Organic Photoreceptors for Imaging system.* New York: Marcel Dekker.

P.E. Burrows, Z. S. V. B. D. M. M. s. R. F. e. a., 1996. Relationship between electroluminescence and current transport in organic heterojunction lightemitting devices. *Journal of applied Physics,* 79(10), pp. 7991-8006.

R. R Lunt, N. C. G. A. A. J. B. B. S., 2009. Exciton diffusion lengths of organic semiconductor thi filmmesured by specially resolved photoluminescence quenching. *Jounal of Applied Physics,* Volume 105, pp. 053711-1-7.

S Reineke, M. T. B. L. a. K. L., 2013. White organic light-emitting diodes; Status and perspective. *Reviews of modern Physics,* Volume 85, p. 1245.

S. Reineke, F. L. g. S. N. S. K. W. B. L. a. K. L., 2009. White organic light-emitting diodes with fluorescent tube efficiency. *Nature,* Volume 459, pp. 234-239.

Bibliography

S. Reineke, k. W. a. K. L., 2007. triplet-exciton quenching in organic phosphorescent light-emitting diodes with Ir-based emitters. *Physical Review B,* Volume 75, p. 125328.

S. Reineke, M. A. B., 2012. Recent Progress in the Understanding of Exciton Dynamics within Phopsphorescent OLEDs. *Physica status solidi (a),* 209(12), pp. 2341-2353.

S. Su, E. G. H. S. J. K., 2008. Highly efficient organic blue- and white-light-emitting devices having a carrier-amd exciton-confining structure for reduced efficiency roll-off. *Advanced Materials,* 20(21), pp. 4189-4194.

S.L. M. van Mensfoort, V. S. R. J. d. V. R. A. J. J. a. R. C., 2010. Hole transport in the organic small molecule material a-NPD: evidence for the presence of correlated disorder. *Journal of Applied Physics,* Volume 107, pp. 113710-1-8.

S.M.Sze, 1981. *Physics of Semiconductor Devices.* New York: Wiley.

S.Reineke, F. L. G. S. N. S. K. B. L. ,. a. K. L., 2009. white organic light-emitting diodes with fluorescence tube efficiency. *Nature,* Volume 459, pp. 234-238.

T. Chen, L. Z. J. Y. Z. A. r. C. Y. T. H. L. X. X. a. W. H., 2015. Understanding the Control of Singlet-Triplet splitting for Organic Exciton Manipulating: A Combined Theoretical and Experimental Approach. *Scientific Report,* Volume 5, p. 10923.

T. Förster, 1948. Zwischenmolekulare Energiewanderung und Fluoreszenz. *Annalen der Physik,* 2(55).

Thompson, M., 2007. The Evolution of Organometallic Complexes in Organic Light-Emitting Devices. *MRS Bullettin,* 32(9), pp. 694-701.

Tsormpatsidis, E. H. R. D. F. B. N. H. P. W. A., 2008. UV irradiance as a major influence on growth, development andsecondary product of commercial importance in Lollo Rosso lettuce'Revolution' grown under polyethylene films.. *Environ. Exp. Bot.,* Volume 63, p. 232–239.

V. Bulovic, a. S. M. B. E. B. V. G. K. M. E. T. a. S. F., 1998. Bright, saturated, red-to-yellow organic light-emitting devices based on polarization-induced spectral shifts. *Chemical Physics Letters,* 287(3-4), pp. 455-460.

W. Brütting, S. B. A. G. M., 2001. Device physics of organic light-emitting diodes based on molecular materials. *Organic Electronics,* Volume 2, pp. 1-36.

Bibliography

W. Helfrich, W. G. S., 1965. Recombination Radiation in Antracene Crystals. *Phys. Rev. Lett,* 14(229).

W.F. Pasveer, e. a., 2005. Undefied Description of Charge-Carrier Mobilities in Disordered Semiconducting Polymers. *Physical Review Letters,* Volume 94, p. 206601.

Y. Jang, J. K. a. D. B., 2013. Invisible metal-grid transparent electrode prepared by electrohydrodynamic (EHD) jet printing. *J. Phys. D: Appl. Phys.,* Volume 46 , pp. 155103-1-5.

Y. Kawamura, a. a., 2005. 100% phosphorescence quantum efficiency of Ir(III) complexes in organic semiconductor films. *Applied Physics Letters,* 86(7).

Y.R. Sun, N. C. G. H. K. B. M. M. T. a. S. R. F., 2006. Management of singlet and triplet excitons for rfficent white organic light-emitting devices. *Nature,* Volume 440, pp. 908-912.

Y.R. Sun, N. C. G. H. K. B. W. M. M., n.d.

Yersin, H., 2004. Transition Metal and Rare Earth Compounds III. Volume 241.

Bibliography

Appendix A1

Defining $n(x)$ as the electrons concentration in the α-NPD layer, where x is the distance inside the α-NPD from the interface α-NPD÷SimCp where the electrons are injected, and $\tau_n(x)$ the mean lifetime of the electrons (See Figure 19).

According to the Shockley-Read-Hall recombination statistics in steady state, the position-dependent recombination rate of the electrons in the α-NPD, $r(x)$, is then given by:

Eq 31

$$r(x) = \frac{n(x)}{\tau_n(x)};$$

where $n(x)$ is the electrons density and $\tau_n(x)$ is the mean lifetime of electrons in the LUMO energy level.

Combining the steady-state continuity equation for the electrons in the α-NPD (first equation Eq 32and the electrons current density formulation (second equation in Eq 32):

Eq 32

$$
\begin{cases}
\dfrac{\partial n}{\partial t} = \dfrac{1}{q}\nabla \cdot \vec{J}_n(x) - \dfrac{n(x)}{\tau_n(x)} \\
\vec{J}_n(x) = qD_n \nabla n(x) + q\mu_n n(x)F(x)
\end{cases}
$$

in which D_n is the electrons diffusion constant, μ_n is the electron mobility and $F(x)$ is the position-dependent electric field in the α-NPD.
Assuming this, as a mono-dimensional problem, and taking into account only the x-dependence of the all physical parameter involved, the system of equations in where $n(x)$ is the electrons density and $\tau n(x)$ is the mean lifetime of electrons in the LUMO energy level.

Combining the steady-state continuity equation for the electrons in the α-NPD (first equation Eq 32and the electrons current density formulation (second equation in Eq 32):

Eq 32 can be rewritten as following:

Eq 33

$$\begin{cases} \dfrac{dn}{dt} = \dfrac{1}{q}\dfrac{d}{dx}\big[J_n(x)\big] - \dfrac{n(x)}{\tau_n(x)} \\[3mm] \vec{J}_n(x) = qD_n\dfrac{d}{dx}\big[n(x)\big] + q\mu_n n(x)F(x) \end{cases}$$

Replacing the expression of the current density in the first equation

Eq 34

$$\frac{1}{q}\frac{d}{dx}\left[qD_n\frac{dn(x)}{dx} + q\mu_n n(x)F(x)\right] - \frac{n(x)}{\tau_n(x)} = 0;$$

Under high current injection, drift current dominates (second term in the square bracket):

Eq 35

$$\frac{n(x)}{\tau_n(x)} = \mu_n \frac{d}{dx}\big[n(x)F(x)\big];$$

Previous studies have approximated the electric field (P.E. Burrows, 1996), using the regional approximation (M.A. Lampert, 1970) as following:

Eq 36

$$F(x) \approx \frac{xF(0)}{l} \; ;$$

where l is the thickness of the α-NPD, and $F(0)$ the electric field at the interface α-NPD÷SimCp.

Following a similar approach made by (P.E. Burrows, 1996), the expression of the mean lifetime can be written as:

Eq 37

$$\frac{1}{\tau_n(x)} = \frac{x/l}{\tau_n(l)};$$

Using the assumptions in the Previous studies have approximated the electric field, using the regional approximation as following:

Eq 36 and in the where l is the thickness of the α-NPD, and *F(0)* the electric field at the interface α-NPD÷SimCp.

Following a similar approach made by , the expression of the mean lifetime can be written as:

Eq 37

$$\frac{1}{\tau_n(x)} = \frac{x/l}{\tau_n(l)};$$

, Eq 35 can become:

Eq 38

$$\frac{n(x)x}{\tau_n(l)l} = \mu_n F(0) \frac{1}{l} \frac{d}{dx}[n(x)x]$$

Or rather :

Eq 39

$$n(x)x = \mu_n \tau_n(l) F(0) \frac{d}{dx}[n(x)x];$$

which is a linear differential equation, homogeneous with constant coefficients and it can be solved to yield an approximate expression for *n(x)* valid per *x > 0*, near *x = l*. A way to solve it, is by a parameters changing, using $y = n(x)x$ and imposing $L = \mu_n \tau_n(l) F(0)$. Under these considerations,

Eq 39 become simply:

Eq 40

$$y = L\frac{dy}{dx};$$

whose general solution is:

Eq 41

$$y = C\exp\left(\frac{x}{L}\right);$$

where C is a constant and it is calculated imposing the boundary conditions in $x = l$:

$$y\big|_{x=l} = n(l)l = C\exp\left(\frac{l}{L}\right) \Rightarrow C = n(l)l\exp\left(\frac{-l}{L}\right),$$

then Eq 41 is:

Eq 42

$$n(x) = \frac{n(l)l}{x}\exp\left(\frac{x-l}{L}\right),$$

namely the distribution of the electron density in the α-NPD, where L is the characteristic electron decay length, $n(l) = N_{lumo}exp[-(E_{LUMO}-E_n)/kT]$.

So, using the assumption in Eq 37, the recombination rate of the electrons in the α-NPD, $r(x)$ is:

Eq 43

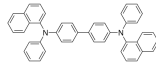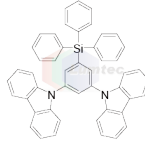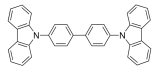$$\frac{n(x)}{\tau_n(x)} = \frac{n(l)}{\tau_n(l)}\exp\left(\frac{x-l}{L}\right).$$
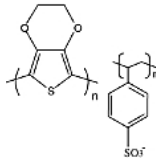
The total recombination rate per unit area is:

$$R = \int_0^l r(x)dx = \int_0^l \frac{n(x)}{\tau_n(x)}dx \Rightarrow \frac{n(l)}{\tau_n(l)}L\exp\left(\frac{x-l}{L}\right)\bigg|_0^l$$
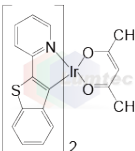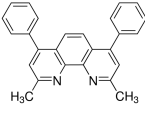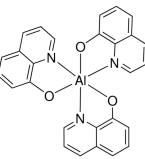
$$R = \frac{n(l)}{\tau_n(l)}L\left[1 - \exp\left(\frac{-l}{L}\right)\right].$$

Appendix A2

This is the list of materials exploited in this thesis. OLED function layer only to the use employed in this work.

Short name	Chemical name	Provider	OLED function layer	Chemical structure
Pedot:PSS	(poly(3,4-ethylenedioxythiophene) polystyrene sulfonate)	Heraeous (P VP Al 4083)	Hole Injection Layer	
α-NPD	*N,N′*-Bis(naphthalen-1-yl)-*N,N′*-bis(phenyl)benzidine	Sigma-Aldrich	Hole Transport Layer/Fluorescent Blue emitter	
SimCp	9,9'-(5-(Triphenylsilyl)-1,3-phenylene)bis(9H -carbazole)	Luminescence Technology Corp.	Phosphorescent Host material	
CBP	4,4′-Bis(9-carbazolyl)-1,1′-biphenyl, 4,4-*N,N′*-Dicarbazole-1,1′-biphenyl	Sigma-Aldrich	Phosphorescent Host material	

Ir(btp)2(acac)	Bis(2-benzo[b]thiophen-2-yl-pyridine)(acetylacetonate) iridium(III)	Luminescence Technology Corp.	Phosphorescent Red dopant	
BCP	2,9-Dimethyl-4,7-diphenyl-1,10-phenanthroline	Sigma-Aldrich	Hole Blocking	
Alq3	8-Hydroxyquinoline aluminum	Sigma-Aldrich	Electron Transport Layer	
TcTa	4,4',4''-Tris(carbazol-9-yl)triphenylamine	Luminescence Technology Corp.	Electron Blocking	